IN-SITU STRESS AND NATURAL FRACTURE NETWORKS IN THE CARNARVON BASIN, NORTH WEST SHELF, AUSTRALIA

THE UNIVERSITY of ADELAIDE

Thesis submitted in accordance with the requirements of the University of Adelaide for an Honours Degree in Geology

Gilby Mats Morrison Jepson

November 2014

IN-SITU STRESS AND NATURAL FRACTURE NETWORKS IN THE CARNARVON BASIN, NORTH WEST SHELF, AUSTRALIA

ABSTRACT

A total of 517 naturally occurring fractures are identified on 12 resistivity image logs in Carnarvon Basin on the North West Shelf of Australia. A range of fracture orientations were present. The fractures can be divided in to two sets using image logs. 1) Electrically resistive and conductive fractures orientated NE-SW, 2) electrically resistive and conductive fractures orientated E-W. There are 235 electrically resistive fractures that are considered to be cemented with electrically resistive cements. These electrically resistive fractures dominantly orientated NE-SW. There are 282 conductive fractures that are considered to be uncemented and filled with drilling mud. Thus, these fractures are considered to be open for fluid flow. The conductive fractures are dominantly orientated E-W.

The in-situ stress field is a major control on the ability for fractures to transmit fluid. 123 drilling induced tensile fractures and 175 borehole breakouts present in 12 image logs, determined a mean maximum horizontal stress orientation of 110°. Leak-off tests and density logs were used to calculate the in-situ stress magnitudes with a vertical stress (S_v) of 21.7 MPa/km, a minimum horizontal stress (S_{hmin}) of 16.8 MPa/km and a maximum horizontal stress of 23.4 MPa/km (S_{Hmax}), this indicates a strike-slip faulting stress regime ($S_{Hmax} > S_v > S_{hmin}$) in the Carnarvon Basin. Using fracture susceptibility plots and Mohr circles constrained by the in-situ stress values, we show that the majority of E-W striking conductive fractures are optimally oriented within the in-situ stress field, demonstrating a high likelihood for fluid transmission. Additionally,

several of these fractures demonstrate significant losses of drilling fluids at corresponding depths. It is likely that the identified conductive fractures are indeed open to fluid flow; demonstrating that these fracture networks provide secondary permeability the Carnarvon Basin subsurface.

KEYWORDS

In-situ Stress, Carnarvon Basin, Natural Fractures, Structural, Geomechanics

TABLE OF CONTENTS

LIST OF FIGURES AND TABLES 4

INTRODUCTION

The Carnarvon Basin is Australia's premier petroleum producing basin, and is the focus of both conventional and unconventional exploration (Figure 1). Unconventional plays (such as coal seam gas, tight gas, and hot sedimentary aquifer geothermal), as well as modern recovery methods, are often heavily reliant on secondary permeabilities provided by natural and enhanced fracture networks (Bell 1996a, Neubauer et al. 2007, Zoback 2010). The formation of natural fractures within rock is dependent on several factors, including the in-situ stress field, rock strength and pore pressure (Anderson 1951, Zoback et al. 1986, Bell 1996b); whilst both pore pressure and rock strength are significant parameters to fracture development, it is magnitude and orientation of in-situ stresses that are often considered to be the most important control over fracture formation (Anderson 1951, Zoback et al. 1986, Bell 1996a).

The in-situ stress regime is defined by the orientation and magnitude of the three principal stresses in the Earth's crust ($\sigma_1 > \sigma_2 > \sigma_3$). These can be resolved into; a vertical stress (S_v), a maximum horizontal stress (S_{Hmax}), and a minimum horizontal stress (S_{hmin}) acting mutually perpendicular upon a single point in the Earth's subsurface (Anderson 1951, Bell 1996a). Fracture formation is driven by the in-situ stress regime, with shear fractures opening 26° to S_{Hmax} and tensile fractures opening parallel to S_{Hmax} (Anderson 1951, Bell 1996b, Healy et al. 2006a). It is widely accepted that fractures aligned to the in-situ S_{Hmax} will be open and have the propensity to conduct fluid (Bell 1996b). However, a recent study by Laubach et al. (2004) has demonstrated that fractures which conduct fluid may not necessarily be aligned to S_{Hmax}.

Over 600 new petroleum wells have been drilled throughout the Carnarvon Basin since 2003. However, these have not yet been used to further characterise sub-surface permeability provided for through natural fractures. This thesis aims to identify natural fractures through the interpretation of wellbore image logs, to determine the presence of fractures and their geometries, orientations, density and connectivity. In addition, in-situ stress orientations and magnitudes are determined. Electrical resistivity and acoustic wellbore images from twelve wells in the Carnarvon Basin were analysed to identify stress indicators such as borehole breakouts (BOs) and drilling induced tensile fractures (DITFs), providing a mean S_{Hmax} orientation of 110°. These same images are used to identify 517 electrically conductive and resistive fractures, encountered in a variety of lithological/stratigraphic units. The magnitudes of the vertical stress (S_v) are also calculated using 15 additional density logs, and the minimum horizontal stress (S_{hmin}) from leak-off tests (LOTs) performed in 35 wells in the Carnarvon Basin.

The 517 natural fractures identified within the wellbores are correlated to the paleo and in-situ stress orientation and their related structural features. Thus, we will determine which fractures are likely to be open and provide fluid flow within the sub-surface under the in-situ stress regime.

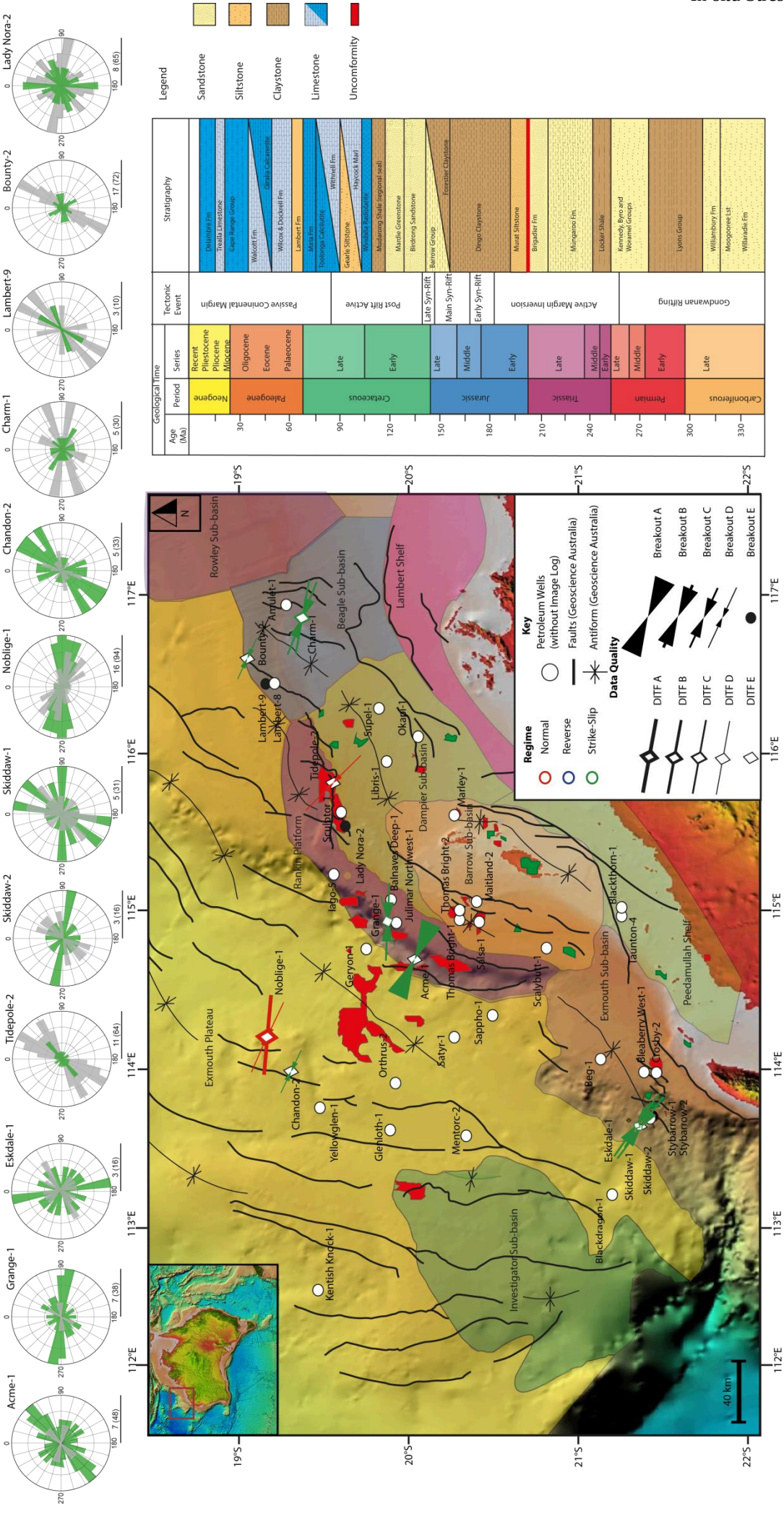

Figure 1: Location map and stratigraphic log of the Carnarvon Basin, indicating structural elements, proven petroleum fields and sub-basin boundaries (Bernecker et al. 2013). The map displays all wells used in the study, along with the 12 wells that provided image logs. Wells with image logs display the orientation of S_{Hmax} provided by both borehole breakouts (BOs) and drilling-induced tensile fractures (DITFs), as well fault regime obtained from stress magnitudes. Fracture magnitude and strike obtained for each of the wells is exhibited in rose diagrams.

BACKGROUND

Geological Setting

The Carnarvon Basin is found on Australia's energy-rich North West Shelf, and is one of the country's principle petroleum producing basins. The Carnarvon Basin is presently a passive continental margin which has an approximately east-west trending strike-slip in-situ stress regime (Hillis et al. 1997, Keep et al. 1998, Tindale et al. 1998, Gartrell 2000).The Carnarvon Basin formed due to initial rifting during the Triassic and a second phase of rifting in the Jurassic (Figure 1, Bernecker et al. 2013).

Basin formation initiated in the Late Carboniferous as Australia began to rift from Gondwana (Felton 1993, Hillis et al. 1997, Longley et al. 2002). Rifting resulted in a set of normal extensional faults striking NE-SW and accommodation space for the basin fill (Longley et al. 2002, Bernecker et al. 2013).

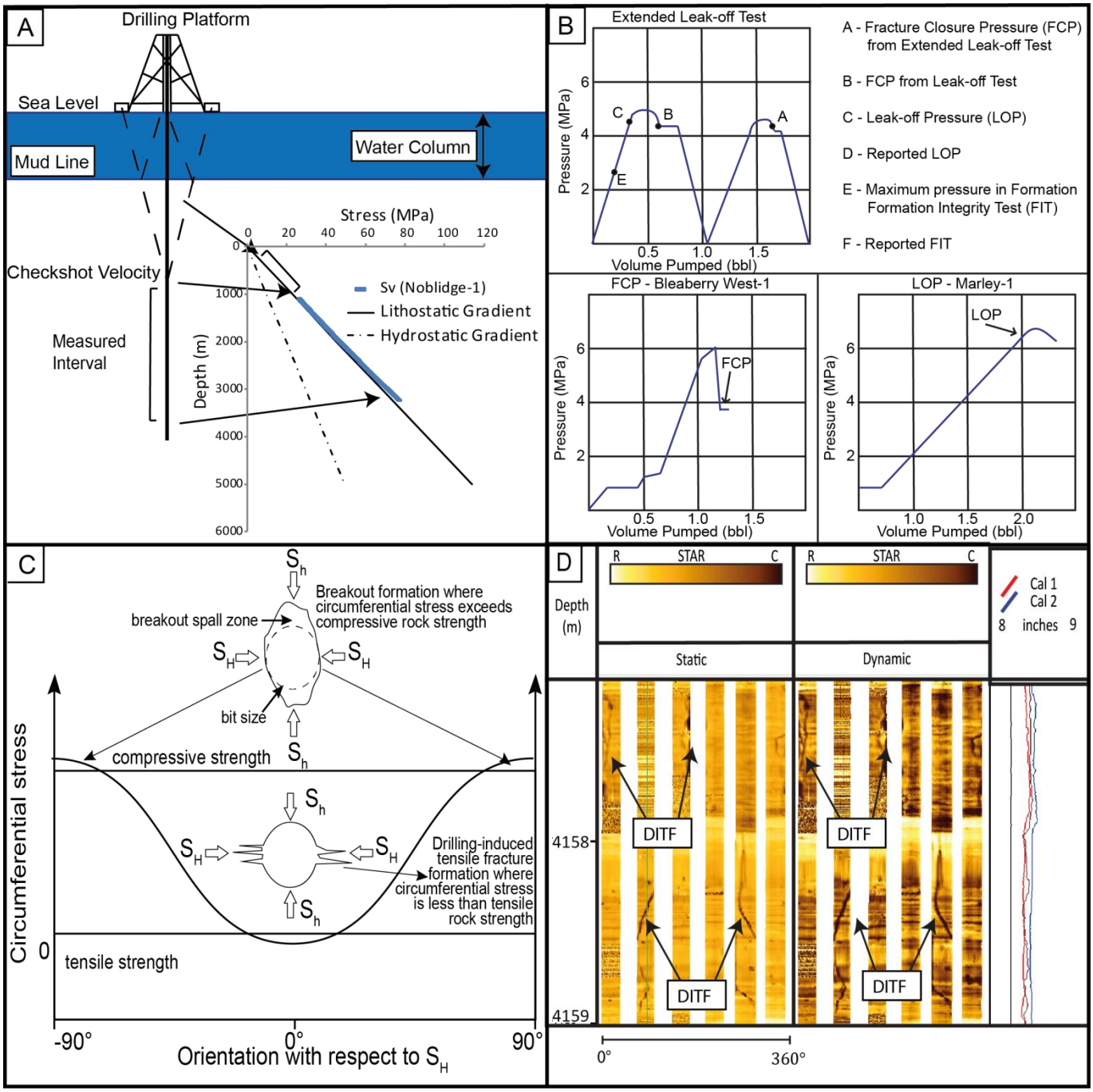

Figure 2: C) A cross-section of a borehole illustrating the postion of borehole breakouts (BOs) and drilling-induced tensile fractures (DITFs) relative to in-situ stress orientation in a vertical wellbore, with the principal stresses (σ1, σ2 and σ3) are displayed as S_H, S_h and S_v. D) A 1:10 scale, static and dynamic, speed corrected Simultaneous Acoustic and Resistivity tool (STAR) image displaying both a BO and DITF (Noblige-1). A) A schematic diagram showing the components of obtaining an estimate for S_v. As density logs are rarely run from surface, in order to determine the top of density log value, the checkshot velocity is used as a proxy to calculate the initial top of log vertical (S_v). B) A pressure versus volume pumped plot, demonstrating Leak-Off Test (LOT) quality, the LOTs are taken from wells; Bleaberry West-1 and Marley-1 (King et al. 2008) .

A period of compression and sag during the Middle to Late Triassic followed, compression resulting in the inversion of the Carboniferous normal faults. A secondary set of NE-SW striking normal faults were generated during the Jurassic rifting phase (Revets et al. 2009). This rifting generated the major hydrocarbon hosting source rocks along with the regional seal for the Carnarvon Basin, the Muderong Shale (Westphal and Aigner 1997, Bishop 1999, Bernecker et al. 2013).

During the Late Cretaceous collision between the Indo-Australia and the Eurasian plate, resulted in convergence and episodic inversion and uplift (Westphal et al. 1997, Tindale et al. 1998, Cathro and Karner 2006). Inversion and tilting continued during the Palaeogene, reactivating underlying Jurassic and Cretaceous basement faults (Audley-Charles et al. 1988, Keep 1998, Tindale et al. 1998). During the Miocene, inversion anticlines formed as fault propagation folds above inverted normal faults (Keep 1998, Cathro et al. 2006). The present-day Carnarvon Basin is likely dominated by a strike-slip faulting stress regime (Neubauer et al. 2007); however neotectonic evidence, such as sea floor doming, suggests that compression is ongoing (Hillis et al. 2008, Revets et al. 2009).

INTERPRETATION OF GEOPHYSICAL LOGS AND WELL TESTS

Image and conventional wireline logs are tools that are used to provide data for the subsurface rock and fluid properties. A range of geophysical logs are utilised, from those that directly measure the borehole conditions and well fluids (e.g. caliper logs, circulation pressure) to those that measure the physical properties of the rock and formation fluids (e.g. density, gamma ray and resistivity). Included in this second class of geophysical logs are image logs (Zoback 2010, Rider and Kennedy 2011).

This study has used three image logs tools: 1) Oil-Based Micro Imager (OMBI); 2) Extended Range Micro Imager (XRMI) and; 3) Simultaneous Acoustic and Resistivity tool (STAR). Both STAR and XRMI are electrical resistivity tools that use water-based drilling mud (Rider et al. 2011). While OBMI is an electrical resistivity tool that uses oil-based drilling mud (Rider et al. 2011). All three tools operate by monitoring the contact resistance of an array of electrodes pushed against the wellbore wall, the data recorded can be processed to give a continuous, vertical pseudo-image for the desired interval (Zoback 2010). These wellbore tools allow for the direct imaging of the distribution and orientation of fractures at depth, as well as being able to identify wellbore failure such as borehole breakouts (BOs) and drilling-induced tensile fractures (DITFs, Zoback et al. 2003).

Image Processing

The wellbore data used in this study was packaged in the Digital Log Interchange Standard (DLIS) format, which is designed for high density magnetic tapes and not hard drives. The DLIS data must be unpackaged in order to be processed and displayed. The

software used to unpack and display the DLIS files was JRS Suite from IKON Science, the JRS Suite contains the necessary tools to process a DLIS file and display an image log from the associated wireline data (Appendix 1).

The JRS Suite software processes the image logs into a speed-corrected pseudo image. Both 'static' and 'dynamic' images are produced. The static image displays a scale contrast of resistivity values based on the variation of resistivity values throughout the entire logged interval; while the dynamic image displays a local scale contrast, through relative resistivity values over a defined window (Rider et al. 2011). In this project all wells displayed satisfactory dynamic image using a 1.0 m window, 0.1 m step, and 64 colours.

IN-SITU STRESS ANALYSIS

The orientation of S_{Hmax} is derived from wellbore failure, such as BOs and DITFs observed in the processed image logs. Stress magnitudes S_v and S_{hmin} are calculated directly from wellbore testing and wireline data. Estimation of S_{Hmax} is the most difficult to constrain and has a number of different methods. In this study S_{Hmax} was indirectly proven using a mathematical relationship with S_{hmin} (Bell 1996a, Brudy and Zoback 1999b). The relative magnitudes of the in-situ stresses with the orientation of S_{Hmax} is used to define the tectonic regime at present-day in the Carnarvon Basin (Anderson 1951, Jaeger and Cook 1979).

A) Acme-1

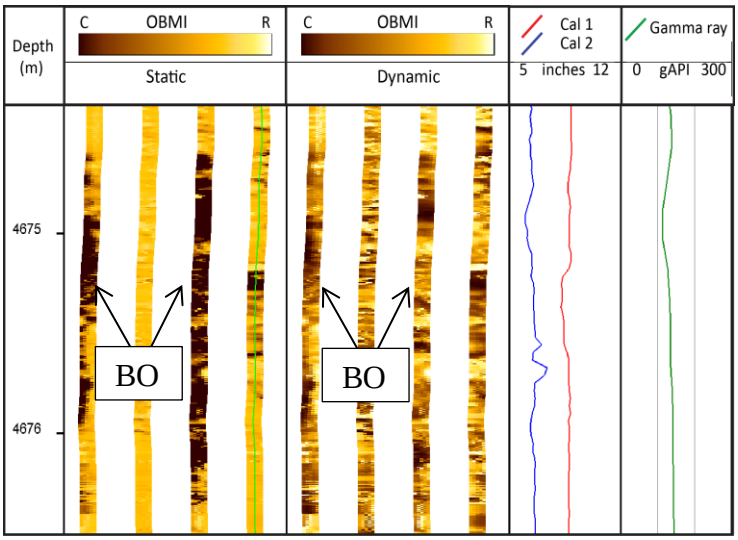

B) Bounty-2

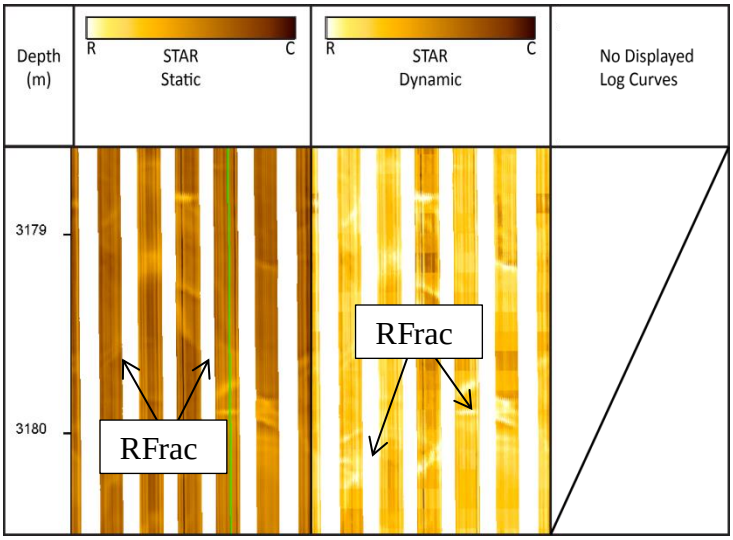

C) Eskdale-1

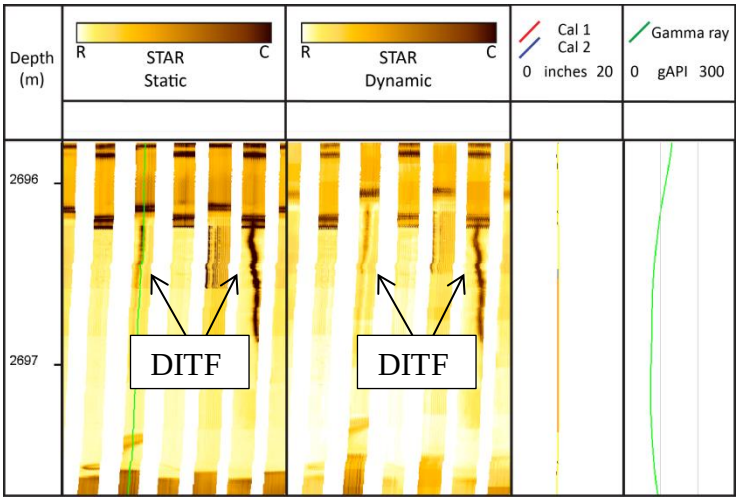

D) Charm-1

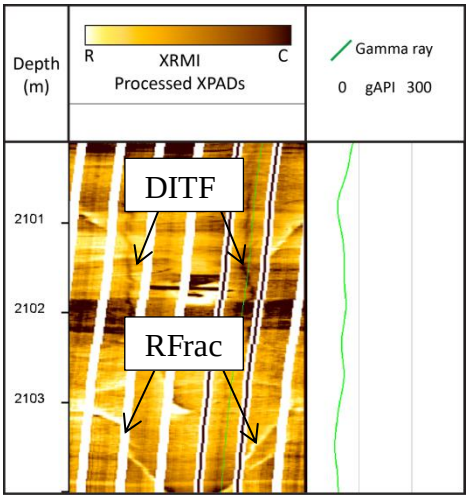

E) Grange-1

F) Noblige-1

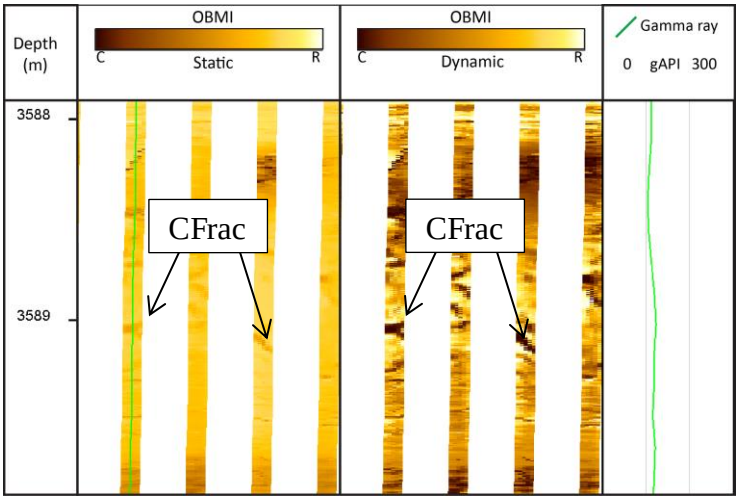

G) Skiddaw-1

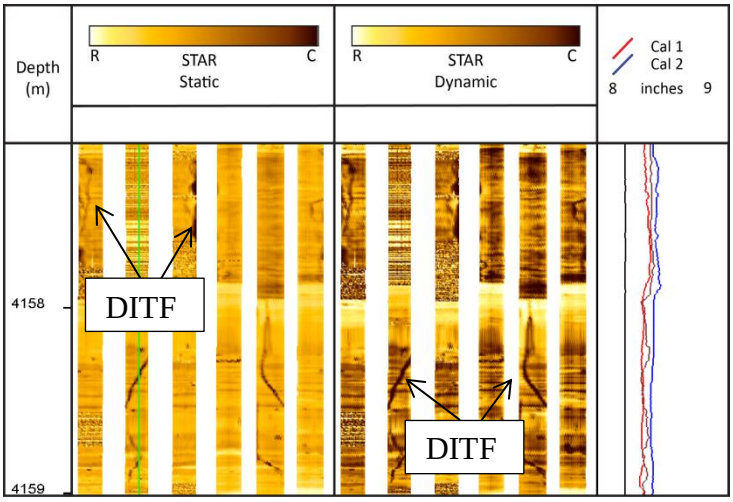

H) Skiddaw-2

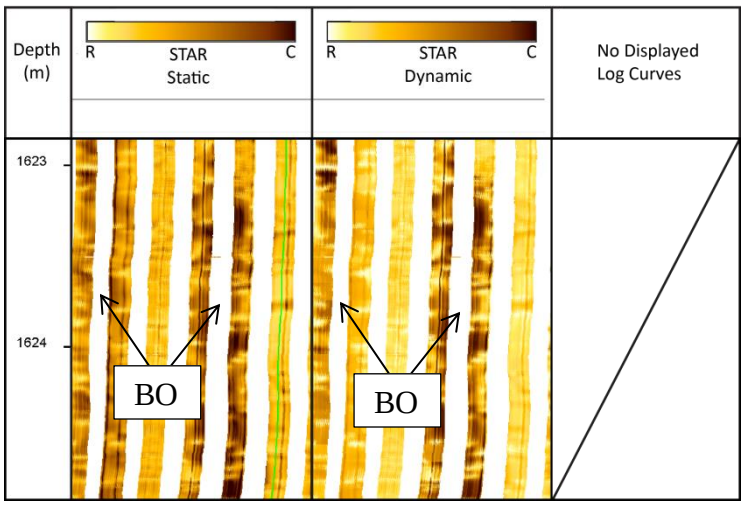

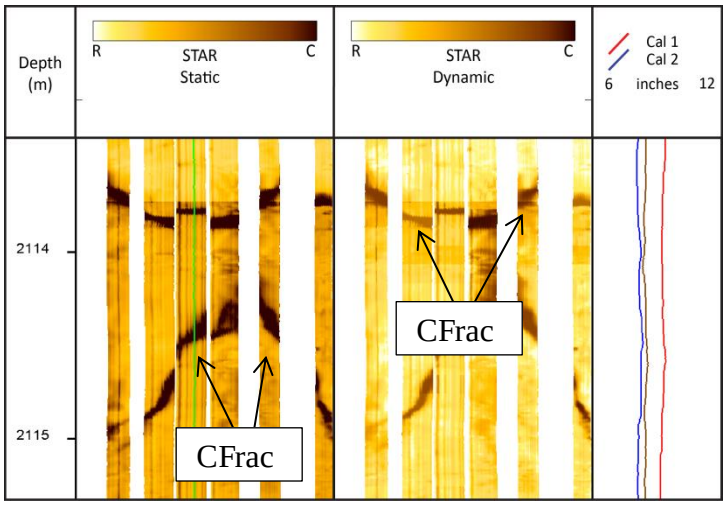

I) Tidepole-2

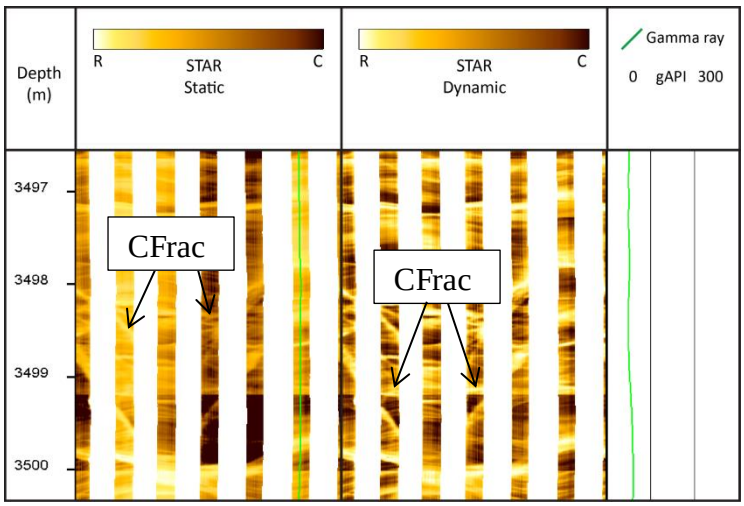

Figure 3: Examples of borehole breakouts (BOs), drilling-induced tensile fractures (DITFs), conductive fractures (CFrac) and resistive fractures (RFrac) displayed as image log features. The wells used are; Acme-1, Bounty-2, Eskdale-1, Charm-1, Grange-1, Noblige-1, Skiddaw-1, Skiddaw-2 and Tidepole-2. Oil-based Micro Imager (OBMI) using an oil-based mud produces an opposite colour scheme to a water-based mud, this is reversed to give a similar, water-based colour scheme.

Maximum Horizontal Stress Orientation

The in-situ stress causes the wellbore to undergo deformation that would not be present in a homogenous, undrilled rock (Zoback et al. 1985, Bell 1996a). Wellbore deformation, BOs and DITFs, can be used to define the in-situ stress (Bell 1996a). A total of 171 BOs and 126 DITFs were identified on image logs from 12 petroleum wells analysed using JRS Suite software (Table 1).

Borehole breakouts are stress-induced elongations of a borehole cross-section which form when the maximum circumferential stress exceeds the compressive strength of the borehole wall. This forms conjugate shear planes that cause pieces of rock to break away and elongate the wellbore in the direction of S_{hmin} (Zoback et al. 1985, Bell 1996a, Hillis et al. 2000). The orientation of the BOs is then used as an indicator for S_{Hmax} (Bell 1996a).

Borehole breakouts are identified on electrical resistivity images as dark, electrically conductive areas separated by 180° (Figure 3). Incipient borehole breakouts can be identified by conjugate shear fractures, these appear as dark ‘crossing’ fractures confined to two areas separated by 180° (Hillis et al. 1998).

The second indicator of the in-situ stress regime is represented by DITFs. Drilling-induced tensile fractures form when the circumferential stress is less than the tensile strength of the borehole wall (Peška and Zoback 1995). Drilling-induced tensile fractures are aligned parallel to the in-situ S_{Hmax} orientation in vertical wells (Hillis et

al. 2000). Occurring as pairs of thin, vertically or near-vertically dipping fractures in the borehole of vertical wells and are separated by 180° (Figure 3; Zoback et al. 2003). Drilling-induced tensile fractures may also be displayed as 'one winged' fractures in the wellbore wall (Barton et al. 1995).

Well (Log Type)	Log Interval (m)	Latitude	Longitude	Indicator Type	n	Total Length (m)	SHmax Orientation (°)	s.d. (°)	Quality
Acme-1 (OBMI)	3300-4714	20.2°S	114.82°E	BO	64	397.5	114.9°N	12.2	A
				DITF	0	0	N/A	0	E
Bounty-2 (STAR)	2852-3795	19.27°S	116.64°E	BO	6	5.2	114.8°N	10.9	D
				DITF	0	0	N/A	0	E
Chandon-2 (OBMI)	2515-3120	19.54°S	114.13°E	BO	0	N/A	N/A	N/A	E
				DITF	0	N/A	N/A	N/A	E
Charm-1 (XRMI)	1540-2232	19.58°S	116.90°E	BO	16	27.7	101.8°N	10.8	C
				DITF	6	21.7	097.8°N	5.7	B
Eskdale-1 (STAR)	2640-3065	21.36°S	113.82°E	BO	0	0	N/A		E
				DITF	25	59.8	119.96°N	33.8	D
Grange-1 (OBMI)	3088-3858	20.08°S	115.09°E	BO	12	31.2	092.5°N	27.4	C
				DITF	5	7.3	074.4°N	14.4	D
Lady Nora-2 (STAR)	2660-3419	19.83°S	115.62°E	BO	2	1.7	142.5°N	0.25	E
				DITF	0	0	N/A	0	E
Lambert-9 (STAR)	3209-2916	19.42°S	116.49°E	BO	3	1.5	125.1°N	22.6	E
				DITF	0	0	N/A	0	E
Noblige-1 (STAR)	2700-4571	19.39°S	114.33°E	BO	15	12.7	103.6°N	28.5	D
				DITF	85	347.5	096.2°N	11.7	A
Skiddaw-1 (STAR)	1504-2180	21.48°S	113.87°E	BO	24	66.6	125.6°N	10.9	C
				DITF	2	3.6	120.3°N	6.1	E
Skiddaw-2 (STAR)	1509-2249	21.48°S	113.87°E	BO	20	28.9	126.8°N	17.4	C
				DITF	3	10.5	127.6°N	13.7	D
Tidepole-2 (STAR)	2880-3660	19.76°S	115.88°E	BO	9	20	135.2°N	16.8	D
				DITF	0	0	N/A	0	E

Table 1: Summary of location, interval, maximum horizontal stress (S_{Hmax}) orientations and standard deviation (s.d.) from borehole breakout (BO), and drilling-induced tensile fractures (DITF) over the twelve wells featuring wellbore resistivity image logs in the Carnarvon Basin. Quality ranking according the World Stress Map (WSM) (Heidbach et al., 2010). Four image log types were used: 1) Oil-Based Micro Imager (OMBI); 2) Extended Range Micro Imager (XRMI) and; 3) Simultaneous Acoustic and Resistivity tool (STAR).

The stress orientation determined for the Carnarvon Basin is 110.2° (Table 1). The World Stress Map (WSM) quality ranking scheme was used to assess the reliability of the wellbore data (Heidbach et al. 2009). Within the WSM classification, stress orientation quality is determined from the number of BOs or DITFs, the total cumulative length of the stress indicator, and the standard deviation (s.d.) from the mean stress orientation (Heidbach et al. 2009). In the original classification scheme, the most reliable quality indicators are labelled A-C, with D and E quality indicators viewed as unreliable stress indicators (Zoback 1992). However, recent studies have shown that D quality indicators can provide reliable estimates of S_{Hmax} orientations for basin and field scale investigations (Tingay et al. 2005, King et al. 2010c).

In this study, BOs were identified in 11 wells, eight wells are ranked A-D and the remaining are E quality. Of the eight reliable wells, one is A quality, four are C quality and two wells are D quality (Table 1). Twelve wells were analysed for DITFs, six of the wells had no or poor DITFs present and thus, assigned an E quality ranking. The five remaining wells display; one A quality, one B quality and three D quality (Table 1).

From interpretation of the A-D quality BOs, the mean regional S_{Hmax} orientation was 114.4° (s.d. of 13.5°). From interpretation of the A-D quality DITF stress indicators, the mean regional S_{Hmax} orientation was 106.2° (s.d. of 18.2°). Therefore the regional in-situ stress of S_{Hmax}, as shown by BOs and DITFs is orientated WNW-ESE.

Pore Pressure Magnitude

Subsurface rocks are filled with fractures and pores, in which fluid phases such as water, air, or hydrocarbons may be stored (Zoback 2010, Rider et al. 2011). If the rock is under a state of compression any pore fluid present influences the stress field. Pore pressure has a direct influence on S_{hmin} by preventing grain compression, decreasing effective stress with an increasing pore pressure (Hillis 2000). Thus, any measurement in an overpressured environment will underestimate S_{hmin}. The effective stress is the stress required to keep a collection of particles rigid, and is equal to:

$$Equation\ 1: \sigma' = \sigma - P$$

Where P is the pore fluid pressure, σ' is the effective stress and σ is the stress acting upon the rock (Jaeger et al. 1979). Changing stress (σ) to effective stress (σ') with the introduction of pore pressure causes the rock to fail more easily, thus, increasing the propensity for fracture formation (Hillis 2000).

Pore pressure was measured directly from 23 petroleum wells in the Carnarvon Basin. The pore pressure was found to fall along the hydrostatic gradient 10.24 MPa per km^{-1} (Figure 4). Several studies, Hillis (2000), van Ruth et al. (2004) and King et al. (2010c), have detailed the presence of overpressure in the Carnarvon Basin, thus, not only is overpressure present, but it also influences S_{hmin} and rock failure. However, the wells sampled the Carnarvon Basin did not indicate presence of overpressure.

Stress Magnitudes

VERTICAL STRESS MAGNITUDE

The vertical stress (S_v) is defined as the stress applied by gravity to any overburden above a specific depth, and therefore is assumed to be vertical (Anderson 1951, Bell 1996a, Zoback 2010). The S_v is calculated through an integration of rock densities measured at each point to the of depth interest (Eq. 2, Bell 1996a, Zoback et al. 2003). Therefore, S_v is expressed as:

$$Eq\ 2: S_v = \int_0^Z \rho(z) g\ dz$$

Where ρ(z) is the density of the overburden at depth z, and g is the acceleration due to gravity (Zoback 2010). As the majority of the Carnarvon Basin is offshore, the water column is included as it contributes to the overburden. An average density of seawater of 1.03gcm^{-1} was used (Bell, 2003). Thus, equation 2 becomes:

$$Eq\ 3: S_V = \rho_w g z_w + \int_{sb}^Z \rho(z) g\ dz$$

where ρ_w is the density of seawater, at a water depth (z_w) and *sb* the depth from seabed (Zoback et al. 1986, Tingay et al. 2003).

In wells that contain a density log that has been run to surface, an accurate vertical stress profile for that well can be directly formulated (Bell 1996a). Majority of density logs are not run from surface, thus, the vertical stress can be calculated from a combination of; a wireline density log run at a given interval and a checkshot survey. A checkshot survey is used to calculate an approximate density of the over-lying sediments if no density log present (Figure 2, Zoback et al. 2003). A checkshot survey

can be used to determine the 'top of log' (TOL, point from which the density log begins) stress value. Using a TOL the vertical stress profile can be formulated for the interval over which the density log was run (Eq. 3, Ludwig et al. 1970). As a checkshot survey only records a depth and a given travel time, processing is required to determine S_v for the TOL interval. In this study, the Gardner relation was used to give an accurate estimate for the top of the density log interval (Gardner et al. 1974).

$$Equation\ 4\text{: } \rho = 0.31 V_p^{0.25}$$

Where ρ is the density and $V_p^{0.25}$ is the P-wave velocity given in m/s (Gardner et al. 1974).

Twenty-six wells were used to calculate S_v, each well containing a density log for a given interval of interest. For these 26 wells, a checkshot survey was used calibrate TOL. Nine wells did not have a corresponding checkshot velocity; these wells were calibrated using a checkshot velocity from a proximal well. The density logs were filtered for erroneous values; null readings and values less than 1.6 gcm^{-3} and greater than 2.6 gcm^{-3} (these values were assessed to be implausible in a sedimentary basin).

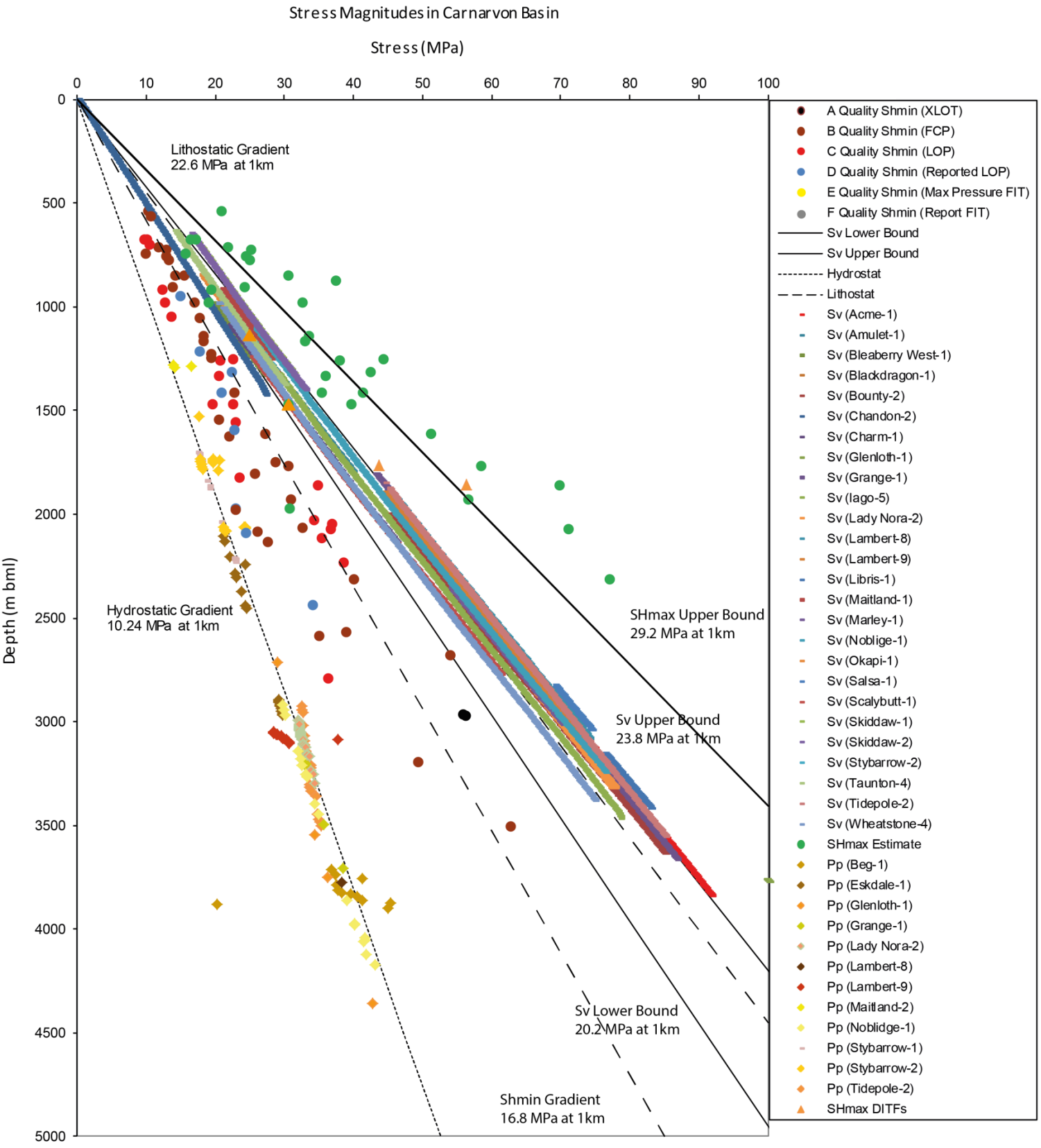

Figure 4: Depth (m) vs stress (MPa) displaying the stress magnitudes of maximum horizontal stress (S_{Hmax}), minimum horizontal stress (S_{hmin}) and vertical stress (S_v) calculated from 26 wells located in the Carnarvon Basin in this study.

Vertical stress profiles were calculated for 26 wells located in the Carnarvon Basin using Equation 2 (Table 2). The vertical stress profile demonstrates a range of gradients, from Chandon-1 at 19.0 MPa km^{-1} to Salsa-1 at 24.4 MPa km^{-1}, giving a range of 5.4 MPa km^{-1} (Figure 4).

Minimum Horizontal Stress Magnitude

The minimum horizontal stress in the Carnarvon Basin was derived directly from 35 wellbore tests performed during the drilling. The magnitude of S_{hmin} is estimated from fracture closure pressure (FCP) and leak-off pressure (LOP), which are obtained through hydraulic fracturing tests, such as leak-off tests (LOT) and extended leak-off tests (XLOT, Bell 1996a).

These tests involve the fracturing of an isolated section of fresh wellbore rock while drilling. Drilling fluid is pumped into the isolated wellbore section at a constant rate until a fracture is initiated (Bell 1996a). The formation of a fracture results in a drop in pressure caused by 'leak-off' which provides a minimum estimate for S_{hmin}. This is demonstrated graphically by a change in the slope on a pressure-time plot (Figure 2). The hydraulic fracture formed remains open until S_{hmin} becomes greater than the wellbore pressure, causing the fracture to close (FCP). The FCP provides the most reliable estimate of S_{hmin}, if the LOT is not run to closure, then the LOP can be used to generate a less-reliable estimate of S_{hmin} (Bell 1996a). If the LOT is not completed, the

pressure measurement obtained is known as a formation integrity test (FIT, Figure 2, Bell 2003). This study analysed LOTs from 35 wells located in the Carnarvon Basin to determine a magnitude 16.5 MPa km^{-1} for S_{hmin} (Table-2).

Maximum Horizontal Stress Magnitude

There is no direct method to measure the magnitude of S_{Hmax}; however, it can be derived from the relationship between the minimum circumferential stress around the borehole, S_{Hmax}, S_{hmin}, tensile strength, pore pressure and mud weight in vertical wells (Bell, 1996a; 1996b). Hubbert and Willis (1957) state that in vertical wells:

$$Equation\ 5: S_{Hmax} = 3S_{hmin} - P_w - P - T$$

Where P_w is the wellbore pressure (calculated from mud weight), *P* is the pore pressure (which has been shown to be hydrostatic) and T is the tensile rock strength.
Often rock strength data is not obtained for drilled wells and so no value for T can be obtained. However, tensile strength can be assumed to be zero given the presence of identified tensile failure (Brudy et al. 1999b), and so can be simplified to:

$$Eq\ 5: S_{Hmax} = 3S_{hmin} - P_w - P$$

In instances where *P* is unknown (no drill-stem testing or reservoir stress data), hydrostatic pore pressure can be assumed. However, this generally results in an

overestimation of S_{Hmax} (Brudy & Zoback, 1999), but in this instance, we have identified hydrostatic pore pressure it is accurate.

Where no DITFs can be identified, a different method of estimating the magnitude of S_{Hmax} is used. This method is much less accurate than equation 5, and provides a magnitude for S_{Hmax} that can only be used as an upper bound. This is known as the frictional limits equation as it is based on that criterion and defines an S_{Hmax} upper bound as:

$$Eq\ 6: S_{Hmax} \leq 3.12(S_{hmin} - P) + P$$

Although only providing an upper bound for S_{Hmax}, equation 6 is valuable as it better constrains S_{Hmax} where no DITFs are available. Equation 6 in conjunction with the more accurate DITF equation (Eq 5) provides an accurate constraint on S_{Hmax}.

DITFs were identified in seven wells in this study. Five contained viable LOTs, thus only these wells could be used to calculate S_{Hmax} (Eq 5, Table 2, Figure 4). Using equation 6, an upper bound was produced the 34 petroleum wells which had an A-D quality LOT and did not have either DITFs or an image log present (Table 2). A mean gradient of 30.3 MPa km^{-1} determined for S_{Hmax} (Figure 4).

Wells	Image Log	Depth (m)	Water Depth (m)	Quality	S_{hmin} (MPa km^{-1})	S_v (MPa km^{-1})	S_{Hmax} (MPa km^{-1})	Stress Regime
Acme-1	OBMI	3164	877.7	B	17.5	20	33.9	SS
Amulet-1	N/A	1114	85.62	N/A	N/A	N/A	N/A	N/A
Balnaves Deep-1	N/A	1611	135.5	N/A	N/A	N/A	N/A	N/A
Beaberry West-1	N/A	1177.1	257.9	D	16.1	19.9	29.5	SS
Beg-1	N/A	1789	345	C	13.6	N/A	21.5	N/A
Blackdragon-1	N/A	2104	1406.7	B	18.4	23.1	36.7	SS
Blackthorn-1	N/A	660	18.2	C	15.6	N/A	27.8	N/A
Bounty-2	STAR	2200	151.5	C	17.9	22.6	34.9	SS
Chandon-2	OBMI	2050	1168	B	15.6	19.2	28.0	SS
Charm-1	XRMI	1182	81.9	B	16.6	20.2	31.0	SS
Crosby-1	N/A	1020	200	B	18.8	N/A	37.8	N/A
Eskdale-1	STAR	2536	798	B	17.5	N/A	24.3	N/A
Glenloth-1	N/A	2400	1116.5	D	17.4	26.5	33.5	SS
Grange-1	OBMI	2012	177.1	C	18.9	23.8	27.1	SS
Iago-5	N/A	1560	170.7	D	14.9	21.9	25.8	SS
Julimar Northwest-1	N/A	1525.7	220	C	15.6	N/A	27.9	N/A
Kentish Knock-1	N/A	1944	1227.7	B	13.9	N/A	22.5	N/A
Lady Nora-2	STAR	2077	75	C	17.1	23	32.6	SS
Lambert-8	N/A	1712	130	B	17.1	23.9	32.7	SS
Lambert-9	STAR	2030	131	B	16.3	23.3	30.0	SS
Libris 1	N/A	806	68.3	B	17.8	24.2	34.7	SS
Maitland-2	N/A	1000	58.1	C	13.4	22.6	21.0	NF
Marley 1	N/A	2969.34	43.1	A	19.1	22.9	38.7	SS
Noblige-1	STAR	2749	1312	C	15.6	23.2	12.9	NF
Okapi-1	N/A	679	43.1	C	15.3	21.1	27.0	SS
Salsa-1	N/A	1296	83.8	C	18.6	24.4	37.1	SS
Sappho-1	N/A	1771	819.4	B	17.8	N/A	34.6	N/A
Scalybutt-1	N/A	3472	819.4	B	16.6	20.3	42.7	SS
Skiddaw-1	STAR	N/A	N/A	N/A	N/A	23.8	N/A	N/A
Skiddaw-2	STAR	N/A	N/A	N/A	N/A	23.7	N/A	N/A
Stybarrow-1	N/A	1337	102	C	17.0	N/A	31.1	N/A
Stybarrow-2	N/A	1515	825	B	17.5	21.6	32.2	SS
Supel-1	N/A	1594	862	B	14.0	N/A	34.0	N/A
Taunton-4	N/A	945.15	62.3	C	20.2	21.6	22.8	SS

Thomas Bright-1	N/A	526	18.6	B	16.2	N/A	42.1	N/A
Tidepole-2	STAR	1206	74.7	B	11.8	24	20.4	NF

Table 2: Stress magnitudes recorded for each of the well in this study. Four image logs types are used: 1) Oil-Based Micro Imager (OMBI); 2) Extended Range Micro Imager (XRMI) and; 3) Simultaneous Acoustic and Resistivity tool (STAR). Quality ranking, as defined by the World Stress Map, applied to Leak-Off test acquired for each well (Figure 2B, Zoback 1992, Heidbach et al. 2009). Water depth was subtracted from depth to when calculating stress magnitudes. Majority of wells in this study displayed a strike-slip fault regime, with two wells presenting a normal faulting regime. Rows highlighted in red indicate wells with drilling-induced tensile fractures present, thus, providing a better constraint for S_{Hmax} using the tensile fracture equation (Equation 5, Brudy and Zoback 1999a). This is opposed to the non-highlighted rows which display just an upper bound for S_{Hmax} (equation 6).

Five wells with S_{Hmax} calculated from the presence of DITFs, all five displayed a stress gradient less than 30 MPa km^{-1}. Four of the wells estimated S_{Hmax} to be between 20.4 MPa and 27.1 MPa per kilometre. Tidepole 2 displayed the presence of DITFs and thus, used equation 5 to estimate S_{Hmax}, the gradient determined was 12.9 MPa km^{-2} which is anomalously low, however S_{Hmax} was based upon a D quality FIT and cannot be relied on for accuracy.

NATURAL FRACTURE ANALYSIS

Natural fractures and faults form in response to the stress regime and define subsurface secondary permeability, as they can provide permeable conduits for fluids. Generally, when fracture or fault is active it is considered open and hydraulically conductive. Conversely, fractures and faults may act as impermeable barriers to fluid flow when closed, by mineralisation, cementation or clay-smear along faults, other stress insensitivity may also result in hydraulically resistive fractures and faults (Dewhurst et al. 2002, Bjørlykke et al. 2005).

In order to determine which fractures are most likely to be open and hydraulically conducive at present day, it is necessary to understand the orientation and distribution of

fractures within the in-situ stress regime (Barton et al. 1995). In this study, fracture interpretation was undertaken using image log data. The fracture orientation and density, and how these aspects relate to the in-situ stress field are presented below. Fracture analysis of XRMI, OBMI and STAR logs was also achieved using the JRS Suite software.

Fracture Formation

Fractures, along with BOs, DITFs and sedimentary structures can be picked using image logs. Natural fractures appear on an image log as either electrically conductive or electrically resistive (Brudy et al. 1999b). Natural fractures in image logs are identified by continuous or semi-continuous light or dark sinusoids that cross cut the bedding (King et al. 2008). The crest of a sinusoid represents the up dip section of fracture plane and the trough represents the down dip portion of the fracture plane (Barton et al. 1995).

Two types of fracture were identified, 1) electrically resistive fractures, and; 2) electrically conductive fractures. Resistive fractures appear as light, electrically resistive, discontinuous sinusoids that crosscut the bedding. Conductive fractures appear as dark, electrically discontinuous sinusoids that crosscut the bedding. Electrically conductive fractures interpreted in image logs display features that are open and have the propensity to conduct fluid.

Fractures Identified in the Carnarvon Basin

Resistive and conductive fractures were identified in all twelve wells analysed from the Carnarvon Basin, with a total of 235 resistive and 282 conductive natural fractures.

forming two sets; electrically conductive and resistive fractures striking E-W and electrically conductive and resistive fractures striking NE-SW (Figure 5).

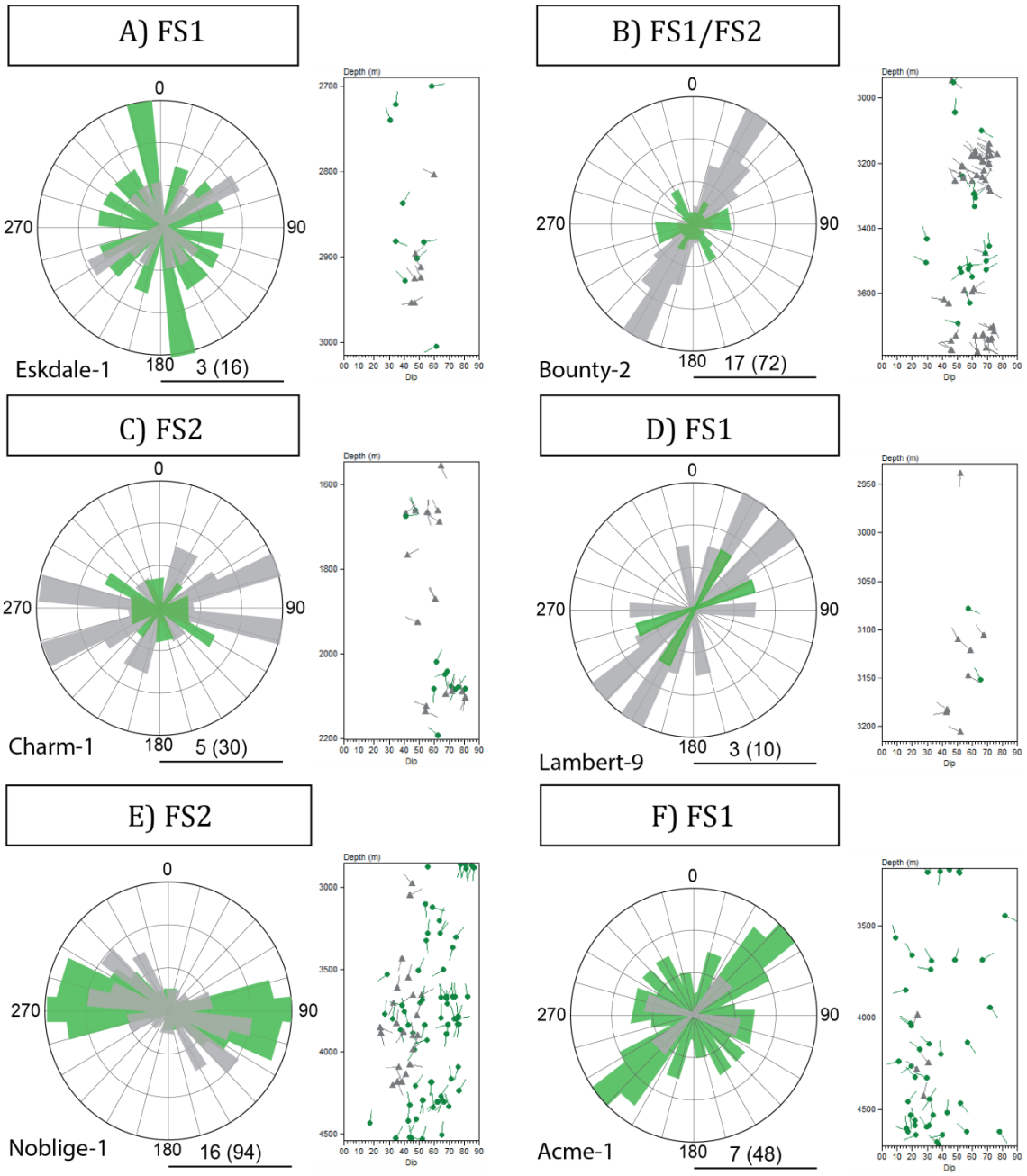

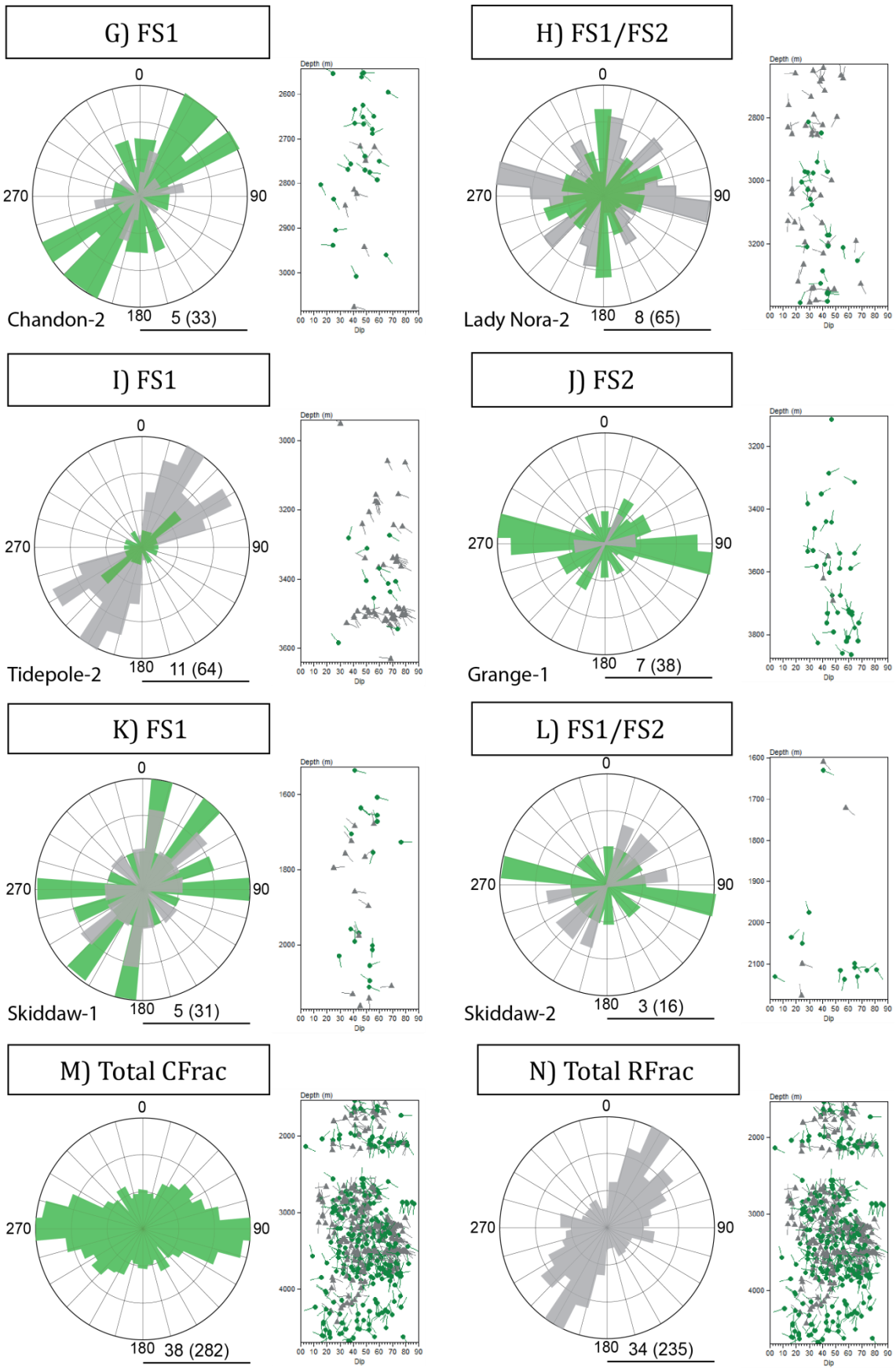

Figure 5: Rose diagrams displaying the frequency and strike of grey resistive fractures (RFrac) and green conductive fractures (CFrac) from the twelve image logs in the Carnarvon Basin. Dip plots display the depth and dip direction of fractures, resistive fractures are displayed as grey tadpoles, with conductive fractures displayed in green tadpoles. Each well is grouped into fracture sets based on the strike of fractures present, fracture set one (FS1) and fracture set two (FS2). Wells with multiple fracture sets present are displayed as: FS1/FS2.

FRACTURE SET ONE (A)

Fracture set one (a) identified in this study is composed of electrically resistive fractures that strike NE-SW. This fracture set is identified in six wells containing 132 electrically resistive fractures identified in the Carnarvon Basin (Figure 5).

Bounty-2 (52) and Tidepole-2 (53) contain the largest NE-SW electrically resistive fracture set. Both Bounty-2 and Tidepole-2 display high density of fractures over specific depths. Identified on Bounty-2 were 30 electrically resistive fractures over a depth interval of 3130-3300, giving a fracture density of 0.17 per m. Tidepole-2 displayed 29 electrically resistive fractures over a depth interval of 3480-3531 m, giving a fracture density of 0.57 per m (Figure 5G). Petroleum wells Eskdale-1 (7), Lambert-9 (8), Skiddaw-1 (4) and Skiddaw-2 (13), all displayed low electrically resistive fractures over the entire wellbore length in the NE-SW orientation (Figure 5).

FRACTURE SET ONE (B)

Fracture set one (b) consists of conductive fractures orientated NE-SW. This set of conductive fractures is identified in five wells; containing 122 conductive fractures orientated NE-SW (Figure 5).

Of the five wells, only Acme-1 (44) displays the greatest number of uniformly NE-SW striking fractures (Figure 5F). Acme-1 displays 19 fractures over depth interval, 4425-4695 m, giving a fracture density of 0.07 per m. Wells with a smaller magnitude of conductive fractures, Lady Nora-2 (23) and Chandon-2 (26) display no notable fracture density with fractures identified occurring the length of the entire wellbore (Figure 5G, 5H). The remaining two wells, Skiddaw-1 and Tidepole-2, are still accurate along the

NE-SW fracture orientation; however have lower fracture number and lower fracture precision (Figure 5I, 5K).

FRACTURE SET TWO (A)

Fracture set two (a) is composed of electrically resistive fractures that are orientated approximately E-W. This fracture set is observed in three wells, containing 83 resistive fractures identified in the Carnarvon Basin (Figure 5).

There are three wells displaying an E-W electrically resistive fracture set, Lady Nora-2 (42) and Noblige-1 (22) highlight this trend. Lady Nora-2 displays low fracture density, with 19 fractures occurring over depth interval 2635-2870 m, giving a fracture density of 0.08 per m (Figure 5H). While Noblige-1 displays no distinct fracture density, with fracturing occurring the entire length of the wellbore. The remaining well, Charm-1, weakly displays the E-W resistive fracture set.

FRACTURE SET TWO (B)

Fracture set four (b) is defined by electrically conductive fractures with an E-W strike. The E-W fracture orientation displays a high density of electrically conductive fractures, identified in four wells, containing 130 conductive fractures (Figure 5).

Grange-1 and Noblige-1 display the greatest number of E-W striking electrically conductive fractures. The number of electrically conductive fractures for Noblige-1 can be separated into 29 over a depth interval 3660-4000m, and 24 over depth interval 4080-4540m, these give a fracture density of 0.08 per m and 0.05 per m respectively

(Figure 5E, 5J). Grange-1 shows 34 conductive fractures over the entire wellbore interval 3056-3873m. Bounty-2 displays a moderate E-W conductive fracture correlation, with 15 conductive fractures over depth interval of 3235-3560m, a fracture density of 0.05 per m (Figure 5B).

LITHOLOGICAL CONTROL AND FRACTURE DENSITY

The mechanical and stratigraphic properties of a rock has long been studied as a control on fracture occurrence (Gross et al. 1995). Recent work by Laubach et al. (2009) has shown that although changing rock properties may exert a control on the formation of fractures. Fractures are likely to form due to the environment at the time and may not take the present day rock properties into consideration. In this study, an investigation of lithology was undertaken at each location a natural fracture was encountered. This was completed by using both the geological reports in the WCR and gamma ray logs available in digital format.

In the Carnarvon Basin, six of the nine wells analysed for lithological control on fractures displayed a higher propensity for natural fractures (both conductive and resistive) to form in units dominated with sandstone as opposed to mudstone or limestone (Table 3).

Fracture				Lithology		
Well	Fracture Set (FS)	Frac Type	n	Mudstone	Sandstone	Limestone
Acme-1	FS1	RFrac	2	3	8	0
		CFrac	44	14	19	0
Bounty-2	FS1/FS2	RFrac	52	1	48	0
		CFrac	20	3	5	0
Chandon-2	FS1	RFrac	7	2	1	5
		CFrac	26	11	1	14
Charm-1	FS2	RFrac	19	N/A	N/A	N/A
		CFrac	11	N/A	N/A	N/A
Eskdale-1	FS1	RFrac	7	1	6	0
		CFrac	9	4	5	0
Grange-1	FS2	RFrac	2	N/A	N/A	N/A
		CFrac	36	N/A	N/A	N/A
Lady Nora-2	FS1/FS2	RFrac	42	29	12	0
		CFrac	23	7	16	0
Lambert-9	FS1	RFrac	8	1	7	0
		CFrac	2	1	1	0
Noblige-1	FS2	RFrac	22	7	15	0
		CFrac	72	21	33	0
Skiddaw-1	FS1	RFrac	13	N/A	N/A	N/A
		CFrac	18	N/A	N/A	N/A
Skiddaw-2	FS1/FS2	RFrac	13	N/A	N/A	N/A
		CFrac	4	N/A	N/A	N/A
Tidepole-2	FS1	RFrac	53	4	38	0
		CFrac	11	1	2	0
Total		RFrac	235	48	135	5
		CFrac	282	62	82	14

Table 3: Attributes of conductive and resistive fracture sets (CFrac and RFrac). Lithological control found for fractures for each well with a lithology report or gamma ray log. Fractures are more likely to be found in lithologies containing sandstone units, however Lady Nora-2 shows that fractures are more likely to be found in mudstones, while Chandon-2 displays a greater number of fractures in limestone units. Not all fractures found are displayed in this table, as no lithological record was acquired for that depth. Number of fractures (n) are separated into; fracture set one (FS1) and fracture set two (FS2). Multiple fracture sets in the same well are denoted by; FS1/FS2

DISCUSSION

Maximum Horizontal Stress Orientation

The orientation of the in-situ S_{Hmax} in the Carnarvon Basin is defined by BOs as, to be 114.4° (s.d. of 13.5°) and by DITFs as 106.2° (s.d. of 18.2°). The two measurements were combined and herein will be described as a single S_{Hmax} orientation of 110.2° (s.d. of 16.6°, Appendix 1).

The in-situ stress orientations from 12 image logs herein are ranked using the World Stress Map (WSM) quality ranking scheme (Heidbach et al. 2009). Six D quality indicators were identified, generally these are considered unreliable regional stress indicators (Zoback 1992). However, Tingay et al. (2005) and King et al. (2010a) demonstrated that D quality wells are capable of giving an accurate orientation of S_{Hmax} for offshore wells in Brunei. The S_{Hmax} orientation based on A-C quality wells alone in the Carnarvon Basin is 107.9° (s.d. of 13.2°), expanding this to include D quality wells (A-D quality), the orientation changes to 110.2° (s.d. of 16.6°). The consistent S_{Hmax} orientation in the two calculations implies that D quality stress indicators can be considered reliable S_{Hmax} orientations in this case.

More recent studies of the in-situ stress regime of the Carnarvon Basin have been completed by Mildren (1997), Neubauer et al. (2007) and Bailey et al. (in review). Mildren (1997) defined S_{Hmax} as 101°, this lies within one s.d. of S_{Hmax} orientation obtained in this study. Mildren (1997) used caliper logs to determine the orientation of S_{Hmax} which provide a lower quality S_{Hmax} indicator (Heidbach et al. 2009). Image logs provide greater detail regarding the size of BOs as well as allowing for the

identification of DITFs, which were not previously possible using caliper logs (Brudy et al. 1999b). This may account for the deviation between the in-stress orientation shown by Mildren (1997) and the orientation determined in this thesis.

The in-situ stress orientation defined by this study has closer parallels to similar image log stress orientation work completed in the Carnarvon Basin by Bailey et al. (in review) and Neubauer et al. (2007). Both authors completed studies into the stress regime of the Carnarvon Basin using image logs, determining the orientation of S_{Hmax} to be 113° and 105° respectively. In comparison to the results of this study, Neubauer et al. (2007) and Bailey et al. (in review) results lie within a single s.d. from the S_{Hmax} orientation of 110°.

In general, S_{Hmax} orientations are parallel to absolute plate motion (Richardson 1992). The motion of the Indo-Australian Plate is 38 mmy^{-1} to the north-northeast (Solomon et al. 1975). Thus, S_{Hmax} orientations in the Carnarvon Basin should be parallel or sub-parallel (Coblentz et al. 1995). The east-west orientation of S_{Hmax} determined herein, along with other studies across Australia, indicates that stress in the Indo-Australian Plate are variable and are not parallel to the absolute motion (Mildren 1997, Hillis and Reynolds 2003). The Australian Stress Map (ASM) demonstrates a complex pattern of S_{Hmax} orientations across the continent due to the plate margin of the Indo-Australian Plate (Hillis et al. 2003). Extensional rifting between Australia-Antarctica, coupled with collision in New Guinea and the Himalayas, transpression at the New Zealand margin and slab-pull at the Sumatra-Java and Soloman-New Hebrides trenches (Coblentz et al. 1995, Hillis et al. 1997, Hillis et al. 2003). The plate tectonics, combined with the brittle

continental lithosphere, caused stress rotation from E-W in the Carnarvon Basin to NW-SE in Australia's northern and southern margins (Hillis et al. 1997).

Stress Magnitudes

VERTICAL STRESS MAGNITUDE

The vertical stress gradient was extensively measured in this study. The lower bound S_v of 19.0 MPa km^{-1} and upper bound of 24.4 MPa km^{-1} indicates a range of vertical stress across the Carnarvon Basin. The calculated S_v in this study sits outside the 18.6-21.35 MPa km^{-1} range calculated in Neubauer et al. (2007). The vertical stress range calculated by King et al. (2010c) is similar, finding an S_v range of 20.2-23.8 MPa/km (Figure 8). The average S_v for the Carnarvon Basin at 1 km was 21.7 MPa, where the average S_v at 2.75 km is 63.7 MPa. Vertical stress is often estimated at 1.0 psi/ft in sedimentary basins, generating a less accurate average of S_v (Tingay et al. 2003).

As vertical stress is equivalent to the overburden, the verity of S_v measurements indicates that the density of lithologies encountered are not homogenous. The wells displaying the highest gradients of S_v appear to correlate with structural highs, this may give an explanation to the raised S_v values (King et al. 2010c). Wells displaying high S_v values are Salsa-1 and Glenoth-1, neither well is located in regions of the Carnarvon Basin with especially thick carbonate layers (such as the Rankin Platform), which often have greater densities than sand or shale rocks and may have resulted in the elevated S_v (Longley et al. 2002).

The large range of S_v found through-out the Carnarvon Basin is a result of the Early Miocene to Pleistocene inversion experienced during the ongoing collision of the Indo-Australia Plate with the Pacific and Eurasian plates (King et al. 2010c). The inversion along normal faults, formed during the Jurassic rifting and Cretaceous thermal sag phases, uplifted over-compacted, higher density sedimentary rocks (Cathro et al. 2006). These lithologies appear to be a major driver for the raised values for S_v, wells recording high S_v magnitudes are proximal to major faults and antiforms (Figure 1).

MINIMUM HORIZONTAL STRESS MAGNITUDE

The magnitude of S_{hmin} is the smallest of the three stresses in the Carnarvon Basin; ranging from a maximum of 20.3 MPa km^{-1} at Sappho-1, to a minimum of 11.6 MPa km^{-1} at Tidepole-2. Estimation of S_{hmin} was carried out using A-C quality LOTs and D quality reported LOTs. With only four S_{hmin} estimates as D quality reported LOTs, the variation in stress magnitudes cannot be attributed to poor-quality data. The S_{hmin} magnitudes acquired for the Carnarvon Basin can be assumed to be representative of in-situ stress.

Previous studies into S_{hmin} in the Carnarvon Basin have been completed by Neubauer et al. (2007) and Bailey et al. (in review). Neubauer et al. (2007) found the S_{hmin} gradient to be 15.2 MPa km^{-1}, while Bailey et al. (in review) found the S_{hmin} gradient to be 18.1 MPa km^{-1}. In this study, the average S_{hmin} gradient was found to be 16.8 MPa km^{-1}. This gradient lies between gradients determined by Neubuaer et al. (2007) and Bailey et al. (in review).

As the overpressure increases, the effective stress decreases bringing the rock closure to failure and thus, lowering S_{hmin} (Hillis 2000). Demonstrated herein pore pressure is hydrostatic gradient for these wells. However, there are some isolated pockets of overpressure, most notably identified in Beg-1 (Figure 5). Beg-1 displays a low S_{hmin} gradient (13.5 MPa km^{-1}), the low gradient of S_{hmin} can be attributed to the presence of overpressure.

MAXIMUM HORIZONTAL STRESS MAGNITUDE

The S_{Hmax} average for the Carnarvon Basin was determined using the tensile fracture method (Eq 5). Four of the five wells displaying DITFs were considered reliable indicators, consisting of two C and two B quality LOTs (Table 2). The minimum estimate of S_{Hmax} was 20.4 MPa km^{-1} from Noblige-1; while the maximum estimate of S_{Hmax} was 27.1 MPa km^{-1} from Grange-1, giving a regional S_{Hmax} of 23.4 MPa km^{-1}.

Previous studies into S_{Hmax} in the Carnarvon Basin have been completed by Neubauer et al. (2007) and Bailey et al. (in review). Neubauer et al. (2007) found the S_{Hmax} gradient to be 26.5 MPa km^{-1}, while Bailey et al. (in review) found the S_{Hmax} gradient to be 25.4 MPa km^{-1}. In this study, the average S_{Hmax} gradient was found to be 23.4 MPa km^{-1}. This is lower than gradients determined by Neubuaer et al. (2007) and Bailey (2014, in review).

A suggested control on S_{Hmax} variation is episodic stress, where stress deformation is not constrained to a single event (Blair and Bilodeau 1988). The in-situ stress field may be experiencing episodes of deformation and relaxation. Theorised in Borneo; episodic

stress may be driven by stress regime experienced at the continental margins and transmitted through the crust (King et al. 2010b). A similar influence may be responsible for the variation of S_{Hmax} in the Carnarvon Basin.

IN-SITU STRESS REGIME

The in-situ stress regime is defined by the relative magnitudes of S_{Hmax}, S_v and S_{hmin}. In the Carnarvon Basin, the minimum principal stress (σ_3) is S_{hmin}, the intermediate principal stress (σ_2) is S_v, and the maximum principal stress (σ_1) is S_{Hmax}, defining a strike-slip fault stress regime (Table 4).

Stress	**Gradient (MPa/km)**	**Orientation**
S_v	21.7	Vertical
S_{hmin}	16.8	020.2°
S_{Hmax}	23.4	110.2°

Table 4: Summary of the contemporary stress field in the Carnarvon Basin. The strike-slip stress regime matches that suggested by previous authors (Neubauer et al. 2007, Bailey et al. in review). In this study, 22 wells displayed a strike-slip fault stress regime, however there were two wells that defined a normal fault stress regime.

Tidepole-2 and Noblige-1 display a normal faulting stress regime where $S_v > S_{Hmax} > S_{hmin}$. The estimate of S_{Hmax} for Tidepole-2 is the erroneous low value associated with a poor quality LOT so is discounted here. Noblige-1 was determined using a C quality LOT, therefore, the presence of normal fault stress regime is considered valid. The occurrence of isolated normal fault regimes may be related to episodic stress cycling (Moore and Iverson 2002). The deformation influenced by the Carnarvon Basin is driven by far-flung Indo-Australia Plate stresses, these stresses may be "relaxed" between tectonic pulses, weakening the horizontal stress and allowing the collapse of

sedimentary sequences (King et al. 2010b). Considering its isolated occurrence, this may be responsible for the normal fault regime observed at Noblige-1.

Structural Permeability

Natural fractures provide secondary permeability and pathways for fluid flow in the subsurface (Sibson 1996, Zoback 2010). Two criteria are required to generate secondary permeability; 1) rock failure to form fractures, and 2) for formed fractures to remain open (Jaeger et al. 1979). Rock failure is controlled by the frictional properties and the rock strength, which are altered by applied shear and effective normal stresses (Sibson 1996). There are two fracture sets found in the Carnarvon Basin; the first contains fractures orientated NE-SW, the second contains fractures orientated E-W. Each fracture set comprises of both electrically resistive and conductive fractures.

FRACTURE SET ONE

Fracture set one comprises of electrically resistive and conductive fractures orientated NE-SW. This coincides with major NE-SW striking faults and inversion antiforms that are present in many of the sub-basins in the Carnarvon Basin (Figure 1, Bernecker et al. 2013). During the Jurassic many large-scale normal faults were formed due to rifting of the Lhasa block forming the Carnarvon Basin (Longley et al. 2002). Larger faults have been shown to be made up of the interconnection of smaller fractures (Walsh and Watterson, 1993). Thus, the NE-SW fracture strike can be related to Jurassic rifting, with this relationship identified in several petroleum wells. The occurrence of electrically conductive fractures with a NE-SW strike supports the theory that fractures

not optimally aligned with S_{Hmax} are still viable conduits for subsurface fluids (Laubach et al. 2004).

- Bounty-2, located within the Beagle sub-basin, which is comprised of a series of N-S and NE-SW striking faults (Figure 1). These steep normal faults are the result of Beagle sub-basin formation during the Middle to Late Jurassic and can be clearly identified along 2D seismic lines (Bernecker et al. 2013).
- Tidepole-2 and Acme-1, located on the Rankin Platform, which is a structurally high, shelf margin separating the Dampier and Barrow sub-basins from the Exmouth Plateau, generated by the rotation of sub-basin fault blocks (Bishop 1999, Cathro et al. 2006). The Rankin Platform hosts a series of steep normal faults striking NE-SW (Figure 1).
- Chandon-2, which lies in the Exmouth Plateau, the Exmouth Plateau has a dominant structural orientation between north and northeast (Figure 5, Bernecker et al. 2013).

FRACTURE SET TWO

The second fracture set identified in six wells in the Carnarvon Basin contains electrically conductive and resistive fractures striking E-W (Figure 5). As shear fractures form 26° to S_{Hmax}, the in-situ stress regime that caused shear fracture formation must be orientated WNW-ESE or WSW-ENE (Healy et al. 2006b).

There are two possible regional stresses that have a suitable orientation to generate an E-W striking fracture set. Miocene compression; which drove the inversion of the NE-SW Jurassic normal faults, or the in-situ stress regime; which is defined by this paper as orientated 110° (Cathro et al. 2006). Thus, it can be interpreted that the E-W fracture strike is generated by two stress regimes; either Miocene compression, or the present-day stress field. Petroleum wells in which the E-W fracture strike was identified were in regions that are relatively uninfluenced by large-scale NE-SW faults that dominate the NE-SW fracture set (Figure 1).

- Lady Nora-2 is part of the Rankin Platform fault system. The Rankin Platform is a complex, highly-faulted fault system which could be the major driver for the complex fracture strike displayed (Figure 5).
- Grange-1 is located in an unfaulted section of the Rankin Plateau, and is not proximal to any major structural features (Figure 1).
- This correlation is mirrored at Noblige-1, which is also located in a relatively undeformed section of the Exmouth Plateau (Figure 1).

FRACTURE INFILL

Open fractures become in-filled whilst conducting fluids, mineral-rich fluids move into open fractures and the change of either pressure or temperature triggers the precipitation of minerals (Dewhurst et al. 2002). The NE-SW fracture set displays the highest number of electrically resistive fractures (Figure 5, Table 2). Fractures filled with electrically resistive cement indicate that the subsurface fluids present during fracture formation must have been quartz- and calcite-rich (Laubach et al. 2004). However, there are still

many NE-SW striking fractures that are electrically conductive, and therefore, likely open to fluid flow.

There are two possible mechanisms that could generate a discrepancy between electrically resistive or conductive fractures with a NE-SW strike. Firstly the NE-SW striking electrically conductive and resistive fractures were all formed during the same Jurassic event and the electrically conductive fractures may be due to isolated compartments not experiencing the same subsurface fluids (Zoback 2010). Secondly NE-SW fractures are generated by different tectonic events, with NE-SW strike, experiencing different subsurface fluids. The second mechanism is more plausible as it would account for multiple wells displaying both electrically resistive and conductive fractures with a NE-SW strike (Figure 5). Thus, there were two phases of Jurassic rifting, with two different subsurface fluid compositions. This would also correlate with the two electrically conductive and resistive sets found in the E-W fracture set.

The E-W fracture set displays a greater number of electrically conductive fractures then the NE-SW fracture set. However, there are still fractures that are identified as electrically resistive with an E-W strike. As discussed in the NE-SW fracture set, open fractures are dependent on the type of fluids present in the subsurface (Laubach et al. 2004). Thus, to generate a set of electrically resistive and a set of electrically conductive fractures, there must be either; a mechanism of fluid isolation through compartmentalisation, or two generations of subsurface fluids. There are two generations of E-W orientated stress regime; Miocene inversion and the present-day stress (Cathro et al. 2006). As there are two generations of E-W stress, it is possible

there were two generations of subsurface fluids, one generating an electrically resistive fracture set and a second generating an electrically conductive set.

Electrically conductive fractures in image logs are assumed to be open to fluid flow. This is based upon the theory that the conductive drilling muds move into open fractures allowing for the fracture void to be highlighted (Rider et al. 2011). However, It has been found that 'open' conductive fractures may actually be in-filled with conductive cements such as siderite (Bailey et al. 2013, Olierook et al. 2014). Thus, they would appear as conductive whilst being closed to fluid flow. Drilling fluid losses and gas shows have been identified in four wells in the Carnarvon Basin, these correspond to depths that feature large or high frequency conductive fractures (Figure 5). Drilling fluid losses and gas shows are indicators of open fractures, causing either gas to leak into the wellbore or drilling fluid to escape into the reservoir. If they correlate to heavily fractured depth intervals it is evidence of conductive fractures being open. Thus, in this paper we can assume that conductive fractures identified in the Carnarvon Basin are open to fluid flow.

LITHOLOGICAL CONTROL ON FRACTURES

The propensity for fractures for form in a particular lithology is linked to rock properties. A rock with a greater Poisson's ration (e.g. sandstone) is likely generate brittle deformation, while a rock with a low Poisson (e.g. shale) is likely to deform elastically (Fossen 2010). The likelihood of more brittle deformation in sandstone units in the Carnarvon Basn would account for the greater natural fracture density observed in the sandstones (Table 3). Therefore, sandstones provide higher values of secondary permeability than other lithologies in the Carnarvon Basin.

FRACTURE FORMATION AND REACTIVATION

Secondary permeability networks require fractures to open in the in-situ stress regime and sealed fractures to reopen. Faults and fractures orientated 26° to the 110° S_{Hmax} orientation are most likely to reactivate (Figure 7). Therefore, fractures striking E-W are optimally orientated in the in-situ stress regime.

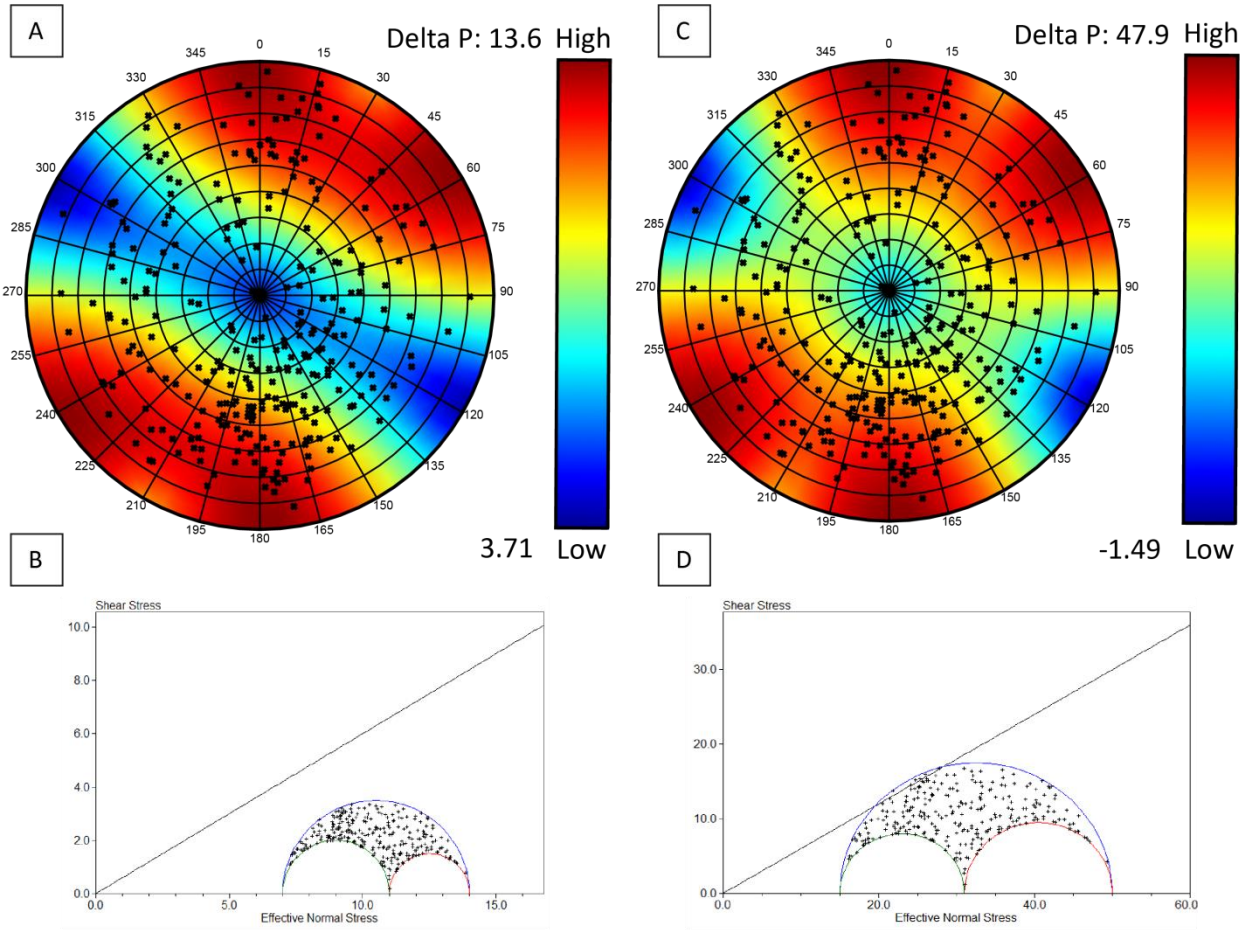

Figure 7: A) Fracture reactivation plot displaying the potential for reactivation of pre-existing faults and fractures in a strike-slip regime at 1 km depth. B) A Mohr diagram displaying which fractures are most likely to fail under the stress magnitudes experienced at 2.5-3.0 km depth. All plots are done with a 0.6 coefficient of friction.

Fractures that are plotted in blue regions have low reactivation potential, these are associated with Jurassic rifting; thus, will be unlikely for fracture re-activation (Figure

7). Mohr diagrams display the likelihood of a rock to fail under a specific stress regime, failure may be generated by two conditions; increase in in-situ stress or overpressure. The Mohr diagram at 1km depth does not indicate a chance of failure; however stresses present at reservoir depth cause the Mohr circle to cross the failure envelope, thus, generating rock failure and fracture formation.

Fracture re-activation along fault zones has long assumed that the failure envelopes for fault rocks can be described by a cohensionless friction law (Byerlee 1978). However more recent work have shown fault networks, such as cemented cataclasites, exhibit far greater cohesive strength than undeformed rocks (Bjørlykke et al. 2005). Dewhurst et al. (2002) in the Carnarvon Basin, has shown that post-deformation lithification due to quartz has increased the cohesive strength of fault rocks. Therefore, generation of new fractures is more likely than the fracture re-activation. Thus, new fractures should form at reservoir depth, with a strike of 084°, approximately E-W.

CONCLUSION

- The orientation of S_{Hmax}, is defined by 123 DITFs and 175 BOs from image logs in 12 wells as, 110°, which is consistent with previous studies in the Carnarvon Basin.
- The magnitude of S_v, is defined by the intergration of density logs at 21.7 MPa km^{-1}. With the magnitude of S_v is controlled by proximity to uplifted structures.
- The magnitude of S_{hmin} is defined as 16.8 MPa km^{-1} using LOT recorded during drilling.

- The magnitude of S_{Hmax} is defined by frictional limits and the relationship of circumfrential stresses and tensile rock strength as 23.4 MPa km^{-1}. With the magnitude of the horizontal stresses controlled by episodic stress cycling.
- The relative magnitudes of the in-situ stresses define a strike-slip fault stress regime ($S_{Hmax} > S_v > S_{hmin}$). However isolated pockets displaying normal fault regime have been identified which are related to sediment sequence collapse during episodic stress cycling.
- Electrically resistive and conductive fractures striking NE-SW are representative of two phases of Jurassic rifting.
- Electrically resistive and conductive fractures striking E-W are representative of Miocene paleostress and the in-situ stress regime.
- Two phases of fluids have interacted with the Carnarvon Basin subsurface generating an electrically resistive cement, one during Jurassic rifting and a second during either Miocene inversion or present-day.
- The optimal orientation for new fracture formation is either 084° or 136° in sandstones at reservoir depth. With existing fractures unlikely to reactivate due to greater cohesive strength.
- With a large portion of total fractures displaying electrically conductive fractures it can be interpreted that; conductive fractures occur in the Carnarvon Basin in an appropriate frequency to enhance subsurface fluid flow.

ACKNOWLEDGEMENTS

I would just like to thank IKON Science for providing the software and the technical support for image log analysis. The Australian Research Council for providing funding and ongoing support for this project, the Western Australian Department of Mines for providing the data to make this project possible, and the Geological Society of Australia SA division for providing assistance to attend the Newcastle ASEC 2014. Finally I would like to thank football, because after a year of honours, there can only be one winner.

REFERENCES

ADDIS M., HANSSEN T., YASSIR N., WILLOUGHBY D. & ENEVER J. 1998 A comparison of leak-off test and extended leak-off test data for stress estimation. *SPE/ISRM Rock Mechanics in Petroleum Engineering*.

ANDERSON E. M. 1951 The Dynamics of Faulting and Dyke Formations. Oliver and Boyd.

AUDLEY-CHARLES M., BALLANTYNE P. & HALL R. 1988 Mesozoic-Cenozoic rift-drift sequence of Asian fragments from Gondwanaland. *Tectonophysics* **155**, 317-330.

BAILEY A., KING R. & HOLFORD S. 2013 Remote Sensing of Subsurface Fractures in the Otway Basin, South Australia. *Journal of Geophysical Research: Solid Earth* **10**, p.22.

BARTON C. A., ZOBACK M. D. & MOOS D. 1995 Fluid flow along potentially active faults in crystalline rock. *Geology* **23**, 683-686.

BELL J. 1996a Petro Geoscience 1. In situ stresses in sedimentary rocks (part 1): measurement techniques. *Geoscience Canada* **23**.

--- 1996b Petro geoscience 2. In situ stresses in sedimentary rocks (part 2): applications of stress measurements. *Geoscience Canada* **23**.

BELL J. S. 2003 Practical methods for estimating in situ stresses for borehole stability applications in sedimentary basins. *Journal of Petroleum Science and Engineering* **38**, 111-119.

BERNECKER T., ROLLET N. & AUSTRALIA G. 2013 The 2013 Offshore Acreage Release for Petroleum Exploration.

BISHOP M. G. 1999 Total Petroleum Systems of the Northwest Shelf, Australia: The Dingo-Mungaroo/Barrow and the Locker-Mungaroo/Barrow. Central Region Energy Resources Team, US Department of the Interior, US Geological Survey.

BJØRLYKKE K., HØEG K., FALEIDE J. I. & JAHREN J. 2005 When do faults in sedimentary basins leak? Stress and deformation in sedimentary basins; examples from the North Sea and Haltenbanken, offshore Norway. *AAPG bulletin* **89**, 1019-1031.

BLAIR T. C. & BILODEAU W. L. 1988 Development of tectonic cyclothems in rift, pull-apart, and foreland basins: sedimentary response to episodic tectonism. *Geology* **16**, 517-520.

BRUDY M. & ZOBACK M. 1999a Drilling-induced tensile wall-fractures: implications for determination of< i> in-situ</i> stress orientation and magnitude. *International Journal of Rock Mechanics and Mining Sciences* **36**, 191-215.

BRUDY M. & ZOBACK M. D. 1999b Drilling-induced tensile wall-fractures: implications for determination of in-situ stress orientation and magnitude. *International Journal of Rock Mechanics and Mining Sciences* **36**, 191-215.

BYERLEE J. 1978 Friction of rocks. *Pure and applied Geophysics* **116**, 615-626.

CATHRO D. L. & KARNER G. D. 2006 Cretaceous–Tertiary inversion history of the Dampier Sub-basin, northwest Australia: Insights from quantitative basin modelling. *Marine and Petroleum Geology* **23**, 503-526.

COBLENTZ D. D., SANDIFORD M., RICHARDSON R. M., ZHOU S. & HILLIS R. 1995 The origins of the intraplate stress field in continental Australia. *Earth and Planetary Science Letters* **133**, 299-309.

DEWHURST D. N., JONES R. M., HILLIS R. R. & MILDREN S. D. 2002 Microstructural and geomechanical characterisation of fault rocks from the Carnarvon and Otway basins. *APPEA journal*.

ENGELDER T. 1993 Stress Regimes in the Lithosphere. Princeton University Press.

FELTON E. A. 1993 Carnarvon Basin, WA. Bureau of Resource Sciences.

FOSSEN H. 2010 Structural geology. Cambridge University Press.

GARDNER G., GARDNER L. & GREGORY A. 1974 Formation velocity and density-the diagnostic basics for stratigraphic traps. *Geophysics* **39**, 770-780.

GARTRELL A. P. 2000 Rheological controls on extensional styles and the structural evolution of the Northern Carnarvon Basin, North West Shelf, Australia. *Australian Journal of Earth Sciences* **47**, 231-244.

GROSS M. R., FISCHER M. P., ENGELDER T. & GREENFIELD R. J. 1995 Factors controlling joint spacing in interbedded sedimentary rocks: integrating numerical models with field observations from the Monterey Formation, USA. *Geological Society, London, Special Publications* **92**, 215-233.

HEALY D., JONES R. R. & HOLDSWORTH R. E. 2006a New insights into the development of brittle shear fractures from a 3-D numerical model of microcrack interaction. *Earth and Planetary Science Letters* **249**, 14-28.

--- 2006b Three-dimensional brittle shear fracturing by tensile crack interaction. *Nature* **439**, 64-67.

HEIDBACH O., TINGAY M., REINECKER J., KURFEN D. & MULLER B. 2009 World Stress Map quality ranking system version 2008 for

contemporary orientation of maximum horizontal compressional stress. *World Stress Map*, p.1.

HEIDBACH O., TINGAY M., BARTH A., REINECKER J., KURFEß D. & MÜLLER B. 2010 Global crustal stress pattern based on the World Stress Map database release 2008. *Tectonophysics* **482**, 3-15.

HILLIS R. 2000 Pore pressure/stress coupling and its implications for seismicity. *Exploration Geophysics* **31**, 448-454.

HILLIS R. R., MILDREN S. D., PIGRAM C. J. & WILLOUGHBY D. R. 1997 Rotation of horizontal stresses in the Australian North West continental shelf due to the collision of the Indo-Australian and Eurasian Plates. *Tectonics* **16**, 323-335.

HILLIS R. R., MEYER J. J. & REYNOLDS S. D. 1998 The Australian stress map. *Exploration Geophysics* **29**, 420-427.

HILLIS R. R. & REYNOLDS S. D. 2000 The Australian stress map. *Journal of the Geological Society* **157**, 915-921.

--- 2003 In situ stress field of Australia. *Geological Society of America Special Papers* **372**, 49-58.

HILLIS R. R., SANDIFORD M., REYNOLDS S. D. & QUIGLEY M. C. 2008 Present-day stresses, seismicity and Neogene-to-Recent tectonics of Australia's 'passive'margins: intraplate deformation controlled by plate boundary forces. *Geological Society, London, Special Publications* **306**, 71-90.

JAEGER J. & COOK N. 1979 Fundamentals of rock mechanics. *Mathuen, London*.

KEEP M., POWELL C. & BAILLIE P. 1998 Neogene deformation of the North West Shelf, Australia. The Sedimentary Basins of Western Australia 2, Proceedings of the Petroleum Exploration Society of Australia Symposium, Perth. pp. 81-91.

KEEP M., POWELL, C.MC.A, & BAILLIA, P.W. 1998 Neogene deformation of the North West Shelf, Australia. In: Purcell, P.G. & Purcell, R.R. (Eds.). *Western Australian Basins Symposium II. Petroleum Exploration Society of Australia (PESA)*, 81–91.

KING R. C., HILLIS R. R. & REYNOLDS S. D. 2008 In situ stresses and natural fractures in the Northern Perth Basin, Australia. *Australian Journal of Earth Sciences* **55**, 685-701.

KING R. C., BACKÉ G., MORLEY C. K., HILLIS R. R. & TINGAY M. R. P. 2010a Balancing deformation in NW Borneo: Quantifying plate-scale vs. gravitational tectonics in a delta and deepwater fold-thrust belt system. *Marine and Petroleum Geology* **27**, 238-246.

KING R. C., HILLIS R. R., TINGAY M. R. P. & DAMIT A. R. 2010b Present-day stresses in Brunei, NW Borneo: superposition of deltaic and active margin tectonics. *Basin Research* **22**, 236-247.

KING R. C., NEUBAUER M., HILLIS R. R. & REYNOLDS S. D. 2010c Variation of vertical stress in the Carnarvon Basin, NW Shelf, Australia. *Tectonophysics* **482**, 73-81.

LAUBACH S. E., OLSON J. E. & GALE J. F. 2004 Are open fractures necessarily aligned with maximum horizontal stress? *Earth and Planetary Science Letters* **222**, 191-195.

LAUBACH S. E., OLSON J. E. & GROSS M. R. 2009 Mechanical and fracture stratigraphy. *AAPG bulletin* **93**, 1413-1426.

LONGLEY I., BUESSENSCHUETT C., CLYDSDALE L., CUBITT C., DAVIS R., JOHNSON M., MARSHALL N., MURRAY A., SOMERVILLE R. & SPRY T. 2002 The North West Shelf of Australia–a Woodside perspective. *The sedimentary basins of Western Australia* **3**, 27-88.

LUDWIG W. J., NAFE J. E. & DRAKE C. L. 1970 Seismic refraction. *The sea* **4**, 53-84.

MILDREN S. 1997 The contemporary stress field of Australia's North West Shelf and collision=-related Tectonism/by Scott D. Mildren.

MOORE P. L. & IVERSON N. R. 2002 Slow episodic shear of granular materials regulated by dilatant strengthening. *Geology* **30**, 843-846.

NEUBAUER M. C., HILLIS R. R., KING R. C. & REYNOLDS S. D. 2007 The contemporary stress field of the offshore Carnarvon Basin, North West Shelf, Western Australia. *Rock Mechanics: Meeting Society's Challenges and Demands, Two Volume Set.* pp. 705-711. Taylor & Francised.

OLIEROOK H. K., TIMMS N. E. & HAMILTON P. J. 2014 Mechanisms for permeability modification in the damage zone of a normal fault, northern Perth Basin, Western Australia. *Marine and Petroleum Geology* **50**, 130-147.

PEŠKA P. & ZOBACK M. D. 1995 Compressive and tensile failure of inclined well bores and determination of in situ stress and rock strength. *Journal of Geophysical Research: Solid Earth* **100**, 12791-12811.

REVETS S. A., KEEP M. & KENNETT B. L. N. 2009 NW Australian intraplate seismicity and stress regime. *Journal of Geophysical Research: Solid Earth* **114**, p.B10305.

RICHARDSON R. M. 1992 Ridge forces, absolute plate motions, and the intraplate stress field. *Journal of Geophysical Research: Solid Earth (1978–2012)* **97**, 11739-11748.

RIDER M. H. & KENNEDY M. 2011 The Geological Interpretation of Well Logs. Rider-French.

SIBSON R. H. 1996 Structural permeability of fluid-driven fault-fracture meshes. *Journal of Structural Geology* **18**, 1031-1042.

SOLOMON S. C., SLEEP N. H. & RICHARDSON R. M. 1975 On the forces driving plate tectonics: Inferences from absolute plate velocities and intraplate stress. *Geophysical Journal International* **42**, 769-801.

TINDALE K., NEWELL N., KEALL J. & SMITH N. 1998 Structural evolution and charge history of the Exmouth Sub-basin, northern Carnarvon Basin, Western Australia. The Sedimentary Basins of Western Australia 2: Proceedings of the Petroleum Exploration Society of Australia Symposium, Perth. pp. 447-472.

TINGAY M. R., HILLIS R. R., MORLEY C. K., SWARBRICK R. E. & DRAKE S. J. 2005 Present-day stress orientation in Brunei: a snapshot of 'prograding tectonics' in a Tertiary delta. *Journal of the Geological Society* **162**, 39-49.

TINGAY M. R. P., HILLIS R. R., MORLEY C. K., SWARBRICK R. E. & OKPERE E. 2003 Variation in vertical stress in the Baram Basin, Brunei: tectonic and geomechanical implications. *Marine and petroleum geology* **20**, 1201-1212.

VAN RUTH P., HILLIS R. & TINGATE P. 2004 The origin of overpressure in the Carnarvon Basin, Western Australia: implications for pore pressure prediction. *Petroleum Geoscience* **10**, 247-257.

WESTPHAL H. & AIGNER T. 1997 Seismic stratigraphy and subsidence analysis in the Barrow-Dampier Subbasin, Northwest Australia. *AAPG Bulletin* **81**, 1721-1749.

WHITE A. J., TRAUGOTT M. O. & SWARBRICK R. E. 2002 The use of leak-off tests as means of predicting minimum in-situ stress. *Petroleum Geoscience* **8**, 189-193.

ZOBACK M., MOOS D., MASTIN L. & ANDERSON R. 1985 Well bore breakouts and in situ stress. *Journal of Geophysical Research: Solid Earth* **90**, 5523-5530.
ZOBACK M., MASTIN L. & BARTON C. 1986 In-situ stress measurements in deep boreholes using hydraulic fracturing wellbore breakouts and stonely wave polarization. ISRM International Symposium. International Society for Rock Mechanics.
ZOBACK M., BARTON C., BRUDY M., CASTILLO D., FINKBEINER T., GROLLIMUND B., MOOS D., PESKA P., WARD C. & WIPRUT D. 2003 Determination of stress orientation and magnitude in deep wells. *International Journal of Rock Mechanics and Mining Sciences* **40**, 1049-1076.
ZOBACK M. D. 2010 Reservoir geomechanics. Cambridge University Press.
ZOBACK M. L. 1992 First- and second-order patterns of stress in the lithosphere: The World Stress Map Project. *Journal of Geophysical Research: Solid Earth* **97**, 11703-11728.

APPENDIX 1: METHODS

Data Acquisition

The data analysed in the Carnarvon Basin was acquired from the Western Australian Department of Mines & Petroleum. Major petroleum companies; Chevron, BHP Billiton, Apache, Santos, Woodside, ENI and Hess have drilled exploration wells throughout the Carnarvon Basin. The well data generated from these wells have been publicly released (year of release) to the West Australian Department of Mines and Petroleum, WA Petroleum and Geothermal Information Management System (WAPIMS) database and used them herein. The drill well data was then downloaded from the WAPIMS database to be further analysed.

Data Format

The well data acquired from WAPIMS in the Carnarvon Basin focused on eight types of wellbore imaging tools, including; Oil-Based Micro Imager (OMBI), X-tended Range Micro Imager (XRMI), Circumferential Borehole Imaging Log (CBIL), Electromagnetic Inspection (EMI), Simultaneous Acoustic and Resistivity tool (STAR), Standard Gamma-Ray (HNGS) and Earthimager-CBIL. In total, 43 wells were available for this study (table 1).

Filtering by these tools, 37 well logs were selected and Digital Log Interchange Standard (DLIS) formatted files for these wells were acquired using the WAPIMS database. Along with DLIS files, Survey, MUD, Logging While Drilling (LWD) and Vertical Seismic Profile (VSP) data as well as Well Completion Reports (WCR) were also collected from the WAPIMS database (Table 2).

Digital Log Interchange Standard files are optimised for high density magnetic tapes and not modern hard drives. As a result, the DLIS files required unpacking before they are processed and displayed.

A number of the DLIS files acquired were either mislabelled or corrupted and showed large sequences of errors when displayed in DLIS InfoView. To correct this issue, the DLIS files were opened in the DLIS to LIS program from the Schlumberger Toolkit. This converted the DLIS files into LIS files. The LIS files were then opened in the LIS to DLIS program from the Schlumberger Toolkit, re-formatting the LIS files back to DLIS files. The newly-formed DLIS files, when opened in the DLIS InfoView (Schlumberger Toolkit), could then be correctly viewed to show the wireline data without error.

Stress Orientation

The formation of structural features within the earth's crust is dependent on the in-situ stress regime being applied to that region. The stress acting on a point can be broken down into three principal stresses; $\boldsymbol{\sigma 1}, \boldsymbol{\sigma 2}$ and $\boldsymbol{\sigma 3}$ (Anderson 1951, Jaeger et al. 1979). The three principal stresses can be further simplified within the earth's crust into two stresses acting in the horizontal plane and one stress acting in the vertical plane (Zoback et al. 1986, Bell 1996a, Zoback 2010). The smallest horizontal stress is known as the minimum horizontal stress ($\boldsymbol{S_{hmin}}$), the largest horizontal stress is known as the maximum horizontal stress ($\boldsymbol{S_{Hmax}}$), and the vertical stress is represented by the vertical stress ($\boldsymbol{S_v}$). This stress representation will be used to describe the three principal stresses ($\boldsymbol{\sigma 1}, \boldsymbol{\sigma 2}$ and $\boldsymbol{\sigma 3}$) further in this thesis and the relative orientations of $\boldsymbol{S_{hmin}}$, $\boldsymbol{S_{Hmax}}$ and $\boldsymbol{S_v}$ determines the stress regime experienced by the earth's crust (Zoback et al. 1985, Bell 1996a).

Minimum Horizontal Stress

The minimum horizontal stress is smallest of the horizontal stresses and acts 90° to the maximum horizontal and vertical stresses. The magnitude of S_{hmin} can only be greater, less than or equal to S_v, as it is constrained by S_{Hmax} (Anderson 1951).

In a drilling environment, the wellbore experiences the influence of the in-situ stress regime (Zoback et al. 1985, Bell 1996a). The in-situ stress causes the wellbore to

undergo deformation that would not otherwise be present in a homogenous, undrilled rock. The deformation experienced by the wellbore is shown in the formation of borehole breakouts (BOs). Borehole breakouts are stress-induced elongations of a borehole cross-section, which form when the maximum circumferential stress exceeds the compressive strength of the compressive strength of the wellbore. This forms intersecting, conjugate shear planes which causes pieces of rock to break of the wellbore and elongate the well bore in the direction of S_{hmin} (Zoback et al. 1985, Bell 1996a, Hillis et al. 2000, Heidbach et al. 2010). The strike of the BOs can be used as an indicator for the orientation of both S_{hmin} and S_{Hmax} (Bell 1996a).

Borehole breakouts were identified on electrical resistivity images as dark, electrically conductive areas separated by 180° (Figure 1). Incipient borehole breakouts can be

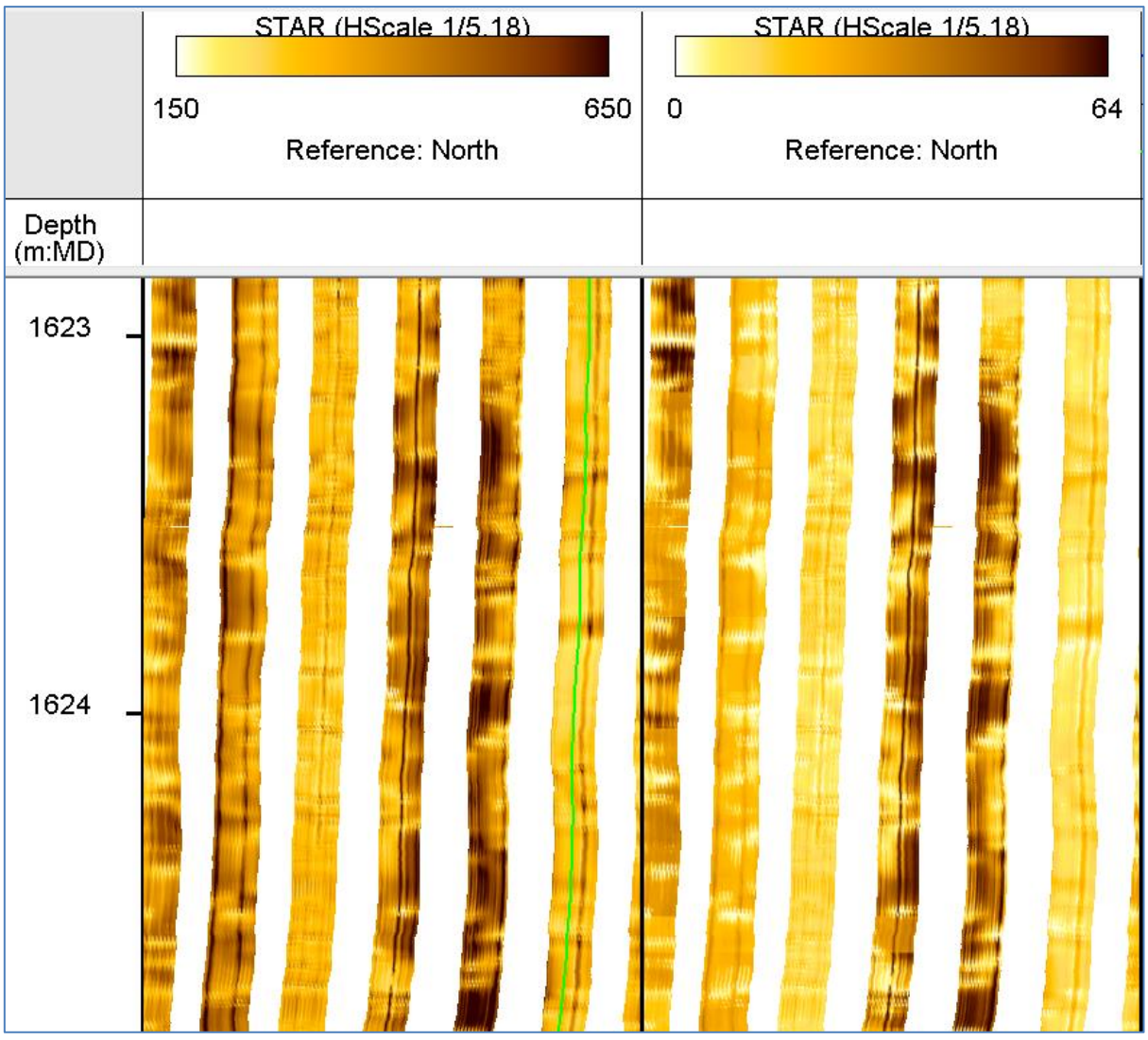

Figure 8: Static and dynamic displays of a STAR image log showing borehole breakouts in a plane view of a 360° wellbore (Hillis and Reynolds 2000).

identified by conjugate shear fractures, these appear as dark 'crossing' fractures confined to two areas separated by 180°.

Maximum Horizontal Stress

The maximum horizontal stress is the largest horizontal principal stress. In a drilling environment S_{Hmax} is displayed by drilling induced tensile fractures (DITFs; Bell 1996a).

Drilling induced tensile fractures form when the circumferential stress is less than the tensile strength of the borehole wall (Peška et al. 1995). Drilling induced tensile fractures are aligned parallel to the in-situ S_{Hmax} orientation in vertical wells (Hillis et al. 2000). Drilling induced tensile fractures occur as pairs of vertically or near-vertically dipping fractures in the borehole of vertical wells and are separated by 180° (Figure 2; Zoback et al. 2003).

On an electrically resistive image log, DITFs appear as dark electrically conductive

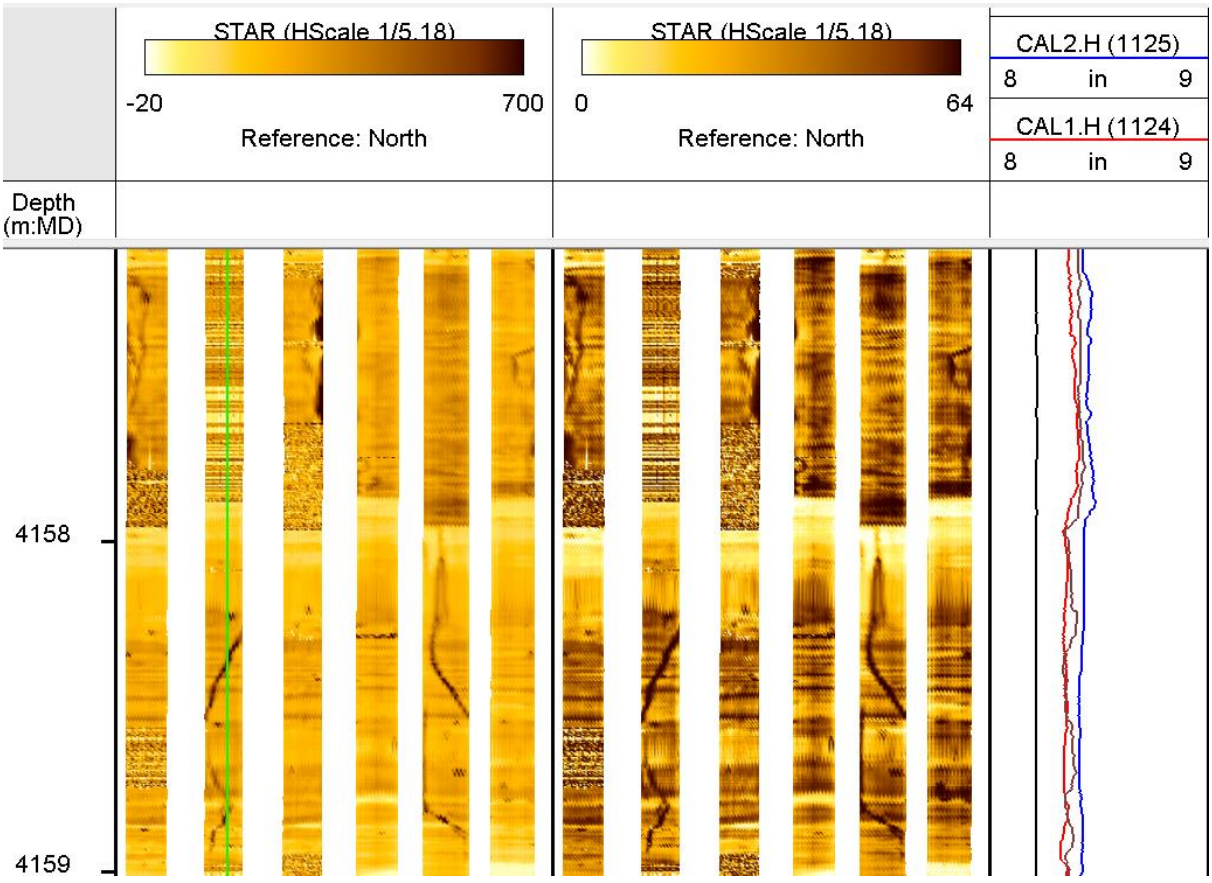

Figure 9: Static and dynamic STAR image log displaying both a drilling induced tensile fracture and a borehole breakout. The image displays a plane view of a 360° wellbore reading.

fractures. Drilling induced tensile fractures tend to be thin, vertical conductive fractures, often with small jogs or kinks. Drilling induced tensile fractures are distinguishable on image logs due to their horizontally discontinuous nature, as they only propagate in the tensile region of the borehole wall (Brudy et al. 1999b). Drilling induced tensile fractures may also form as 'one-winged' features, where only a single vertical fracture is displayed.

Image Log Interpretation

The drilling of the subsurface for geothermal, petroleum or research requires an accurate representation of the basin environment. Tools such as image and caliper logs are used to image the subsurface drilled and provide data and images on the lithologies and features surrounding the wellbore. These tools are placed down a wellbore and are pulled up at a constant pace while recording information about the given interval required. Image logs can then be used to determine the features within the reservoir, such as fractures, stress orientation, bedding and lithology. This study utilised 12 image logs using the image types of Oil-Based Micro Imager (OMBI), X-tended Range Micro Imager (XRMI), Circumferential Borehole Imaging Log (CBIL) and Simultaneous Acoustic and Resistivity tool (STAR).

The data load is gathered from DLIS files which were downloaded from the WAPIMS website. The DLIS files contain the log curves from which the image log can be displayed. The DLIS files are loaded directly into the JRS Suite©. To display the image logs JRS Suite© was used, the JRS Suite© required specific log curves to be present to allow the program to display the image log. These required log curves were different for

each tool (i.e. STAR had a different tool set to OBMI), and a table was used to correlate the DLIS file log curves to the required log curves (Tables 1a, 1b and 1c).

Image data: OMBI		
Log curves		
Log name	**Description**	**Comments**
FCA1-4 FCB1-4 FCC1-4 FCD1-4	Pad data arrays	if not found, no button data exists
FCAZ	tool acceleration	required for processing
ANOR	high resolution accelerometry	
ETIM	elapsed logging time curve	any high resolution elapsed time curve can be used
FTIM	fast channels acquisition time curve	
CS, SPD, LSPD	cable speed curves	required for processing, but can be generated from elapsed time and depth curve

Table 1a: Displays the log curves, log names, description and additional comments about the OBMI log curves required for the JRS Suite© software. Source from IKON Science.

DEVI	hole deviation	required for calculation of real dips
P1AZI P1NO	tool azimuth	required for corrected image correlation
HAZI	hole azimuth	required for calculation of real dips
RB	relative bearing	required for corrected image correlation
C1-C2	caliper arm radius/diameter	required for corrected display image

Field logs		
Log	**Description**	**Comment**
GR	Gamma ray	Useful for interpreting coal intervals
RHOB	Density	

Image Data: STAR		
Log curves		
Log name	**Description**	**Comments**
P1BTN	Pad data arrays	if not found, no button data exists
RAZGST	tool acceleration	required for processing
ETST	elapsed logging time curve	any high resolution elapsed time curve can be used
CS, SPD, LSPD	cable speed curves	required for processing, but can be generated from elapsed time and depth curve
DEVST	hole deviation	required for calculation of real dips
AZST	tool azimuth	required for corrected image correlation
DAZST	hole azimuth	required for calculation of real dips
RBST	relative bearing	required for corrected image correlation
RAD1-6	caliper arm radius/diameter	required for corrected display image

Table 1b: Displays the log curves, log names, description and additional comments about the STAR log curves required for the JRS Suite© software. Source from IKON Science.

Field logs		
Log	**Description**	**Comment**
GR	Gamma ray	Useful for interpreting coal intervals
RHOB	Density	

Image Data: XRMI		
Log curves		
Log curves	**description**	**comments**
XRMIP	processed packed button array	if found, data are processed, collection need to be created
PAD1-6	Pad data arrays	if not found, no button data exists
XPADS	raw XRMI image	not required for interpretation, useful for QC
ZACC	high resolution accelerometry	required for processing
DXTM	high resolution elapsed time curve	any high resolution elapsed time curve can be used
CS SPD LSPD	cable speed	required for processing, but can be generated from elapsed time and depth curve

Table 1c: Displays the log curves, log names, description and additional comments about the XRMI log curves required for the JRS Suite© software. Source from IKON Science.

DEVI	hole deviation	required for calculation of real dips
AZI/AZI1	tool azimuth	required for corrected image correlation
HAZI	hole azimuth	required for calculation of real dips
RB	relative bearing	required for corrected image correlation
CAL1-6 RAD1-6	caliper arm radius/diameter	required for corrected display image
Field logs		
Log	**Description**	**Comment**
GR	Gamma ray	Useful for interpreting coal intervals
RHOB	Density	

All image log processing and initial interpretation was carried out in JRS suite. The Roses module was used to analyse maximum horizontal stress orientations and natural fractures, and to display borehole failure and natural fractures. The Swift module was used to produce fracture susceptibility diagrams.

The following is steps to loading DLIS files into image logs using the JRS Suite.The wireline image log recorded data which was stored on DLIS files, the data required processing to be displayed.

1. The log curves were first checked for any inconsistencies in a data check phase, if all the log curves were applicable the data was then formatted to

produce an image from the log curves present. The major log curves checked were the pad data, caliper logs, tool azimuth, hole azimuth, relative bearing, hole deviation and accelerometry/tool acceleration.

2. The tool acceleration was changed into units of $m/s^2$and displayed in G's. The data was required to be between 0.8 and 1.2, if outside this range (by an order of magnitude), the log curve was divided by the appropriate magnitude of 10.
3. The tool acceleration was then smoothed, in the 'smooth log' tool, by converting it by a unit of 1000. This produced two acceleration curves.
4. To format the data JRS Suite was used, the raw DLIS data is grouped under a single tool identifier which allows it to be formatted.
5. If the data would not show up in the 'data format' phase then the database (Microsoft Access), in which the log curves were accessed through, would have to be edited. The log curves corresponding to the appropriate tools were required to be placed under a single unique tool indicator.
6. Once the log curves were grouped under a single unique tool, the data format process could be undergone.
7. The formatted data could then be added to a collection, the collection was all the tools highlighted in Tables a, b and c under the log name (STAR, OBMI, XRMI). Using this collection, the image log could thus be displayed in an image track within the JRS Suite© image interp program.

8. The image log is required then required to be speed corrected to allow for the various calipers to be aligned. The speed processing involved taking the static log and applying a gravity and speed correction in the JRS Suite to the caliper orientation logs. This was done using the tool acceleration log curves, both smoothed and unsmoothed and applying them to the tool orientation log curves.
9. This gave an output of a speed corrected static image log. The speed corrected static log data can then be processed into a 64 range colour image known as a dynamic log.

To interpret the image log, the static and dynamic logs are displayed together, along with the caliper logs and a gamma ray log. The static and dynamic logs allow for the picking of the wellbore features, while the caliper logs display any change in borehole width or circumference, and the gamma ray log can be interpreted to give the lithology.

Interpretation of the static and dynamic image log for BOs and DITFs is explained in sections **3.1** and **3.2**. These sections are highlighted by adding Frac Zones to the dynamic image on the JRS Suite© image track. The Frac Zone highlights the length and azimuth of the feature, this feature can then be displayed on the JRS Suite© Roses software to determine the orientation of the BO or DITF.

Fractures were broken down into two formats, electrically conductive or electrically resistive. Electrically conductive fractures were displayed as dark sinusoids that typically extend the width of the wellbore. Electrically resistive

fractures were displayed as light sinusoids that typically extend the width of the wellbore. Fractures are picked out using the Sinusoid tool which is added to the dynamic image on the JRS Suite©. When a fracture is picked, the Sinusoid tool provides a sinusoid which can be aligned with the fracture, the fracture is then recorded as being resistive (if light coloured) or conductive (if dark coloured).

An identified natural fracture is marked out using the JRS.exe program and labelled as either a conductive fracture or a resistive fracture. This is compiled in the database for further analysis. Fractures may then plotted in Breakouts JRS Suite© which plots fractures in bins depending on density of fractures at a given orientation, along with the dip and dip direction.

Reyleigh Test

An estimate of the orientation of S_{Hmax} is dependent on the accuracy and precision of the measurements taken. Rather than simply taking an average of the stress orientations, the Rayleigh test was performed, which defines a magnitude in regard to its individual components (Coblentz and Richardson 1995a). Thus, the stress orientation is the magnitude and the individual components are the quality rankings. The Rayleigh test generates both an overall stress orientation and a confidence interval. A confidence interval dictates whether the generated stress orientation is random, or supported by the components. Any weighting that corresponds to a confidence level over 90% confirms that the magnitude is not random. The confidence level for both BOs and DITFs in this study was defined as 99.99%, inferring that the stress orientation determined is not random (Coblentz et al. 1995c, Reynolds et al. 2002).

Stress Magnitudes

As image logs have given the orientation of the in-situ stress regime, a stress magnitude must be calculated for the minimum and maximum horizontal stress, and the vertical stress. The magnitude of these stresses allows to determine the overall, in-situ stress state which is being experienced by the region.

VERTICAL STRESS

The vertical stress magnitude at a specific depth is calculated from the weight of the sediment overburden, as well as the water column for offshore wells (Zoback et al. 2003, Zoback 2010).

To determine the magnitude for vertical stress for a given depth, an integration of rock densities from the surface to the depth required can be calculated. However, majority of density logs are not run from surface (Zoback et al. 2003). Thus the average density from the surface to the top of the well must be calculated from Vertical Seismic Profile (VSP).

The seismic profile is used to determine a Gardner Value, from which S_v at the top of the density log can be calculated (Gardner et al. 1974).

$$\text{Eq 1: } Gardner\ Density\ (g/cm^3) = 1.74 \times Instantaneous\ Velocity\ (km/s)^{0.25}$$

With 1.74 being an empirical value by Gardner 1974 as it is an average density for sedimentary rocks within a basin environment.

$$Eq\ 2: TOL\ Density\ (g/cm^3) = \left(\frac{Depth\ (m)}{Gardner\ Density}\right) \times Top\ of\ Log\ (m)$$

$$Eq\ 3: S_v\ TOL\ (MPa) = Sv(water) + (Gardner\ Density \times 9.8\ \left(\frac{m^2}{s}\right) \times (TOL(km) - Water\ Depth\ (km))$$

$S_v(water\ )$ is the vertical stress if the water column above the base mud level and TOL (Top of Log) being the shallowest depth from which the density log was run. Using the density value calculated for TOL as the initial value for the density log, S_v can be calculated by integration of density log.

$$Eq\ 4: S_v = \int_0^z \rho(z) g\ dz$$

Where ρ(z) is the density of the overlying sediment and water column at depth z, and g is the acceleration due to gravity.

$$Eq\ 5: S_v water = \rho(water) g\ z(water\ depth)$$

$$Eq\ 6: S_v - w = S_v - S_v water$$

MINIMUM HORIZONTAL STRESS

The Minimum Horizontal Stress *(S_{hmin})* is the smallest principal stress in the horizontal plane. The magnitude of S_{hmin} has been determined from the fracture closure pressures (FCP) and leak-off pressures (LOP) gathered from leak-off tests (LOTs) and extended leak-off tests.

These tests involve the fracturing of an isolated section of fresh wellbore rock while drilling. Drilling fluid is pumped into the freshly cut wellbore at a constant rate until a fracture is initiated in the wall of the borehole (Bell 1996a). This is marked by a change in the slope of a pressure-time plot. Fracture closure pressure (FCP) provide the best estimate of S_{hmin} (Bell 1996a).

The calculation of S_{hmin} was performed from the Equivalent Mud Weight (EMW) recorded from the LOTs performed using the following equations (Eq; Jaeger et al. 1979, Engelder 1993).

$$Eq\ 7: S_{hmin}bml(MPa) = \frac{EMW(g/cm^3) \times 1.17676 \times Depth(m) \times 8.335}{1000}$$

$$Eq\ 8: Water\ Stress = \left(\frac{Water\ Depth}{1000}\right) \times 1.05\ (g/cm^3) \times 9.8\ ms^2$$

$$Eq\ 9: S_{hmin} = S_{hmin}bsl - Water\ Stress$$

The most reliable estimates for S_{hmin} come from fracture closure pressures from LOTs, with the least reliable vales for S_{hmin} come from formation integrity tests (Zoback et al. 1986, Bell 1996a, Addis et al. 1998, White et al. 2002).

MAXIMUM HORIZONTAL STRESS

Maximum horizontal stress is the largest principal stress in the horizontal axis. There is no direct method to measure the magnitude of S_{Hmax}; however, it can be derived from the relationship between the minimum circumferential stress around the borehole, S_{Hmax} and S_{hmin}, tensile strength, pore pressure and mud weight in vertical wells (Bell, 1996a; 1996b). Hubbert and Willis (1957) state that in vertical wells:

$$Eq\ 10: S_{Hmax} = 3S_{hmin} - P_w - P_p - T$$

Where P_W is the wellbore pressure (calculated from mud weight), P_p is the pore pressure (which has been shown to be hydrostatic) and T is the tensile rock strength (which is assumed 0 from the presence of DITFs; Brudy et al. 1999b). Often rock strength data is not obtained for drilled wells and so no value for T can be obtained. However, tensile strength can be assumed to be zero given the presence of identified tensile failure (DITFs), and so can be simplified to:

$$Eq\ 11: S_{Hmax} = (3S_v - water) - P_w - P_p$$

for wells featuring DITFs (Brudy & Zoback, 1999). In instances where pore pressure is unknown (no drill stem testing, or reservoir stress data), hydrostatic pore pressure can be assumed. However, this generally results in an overestimation of S_{Hmax} (Brudy & Zoback, 1999).

PORE PRESSURE

Pore pressure is the pressure exerted by fluids within the pore space in rocks in the subsurface. Pore pressure increases with depth along the hydrostatic pressure line in the subsurface assuming that there is permeability and connectivity between the subsurface pore fluids and the surface (Jaeger et al. 1979, Zoback 2010). However is the pore fluids

are isolated, this can cause overpressure, overpressure causes the rocks to be more likely to fail and can lead to incorrect S_{Hmax} and S_{hmin} calculations (Jaeger et al. 1979).
Pore pressure in the wells analysed was determined from drill stem tests (DST), repeat formation tester (RFT) and reservoir characterisation instrument (RCI) acquired from the well completion reports (WCR).

The data obtained from the WCR was frequently given in pounds per square inch or pounds per square inch absolute (PSI and PSIA).

The pressure data was converted to MPa:

$$Eq\ 12: MPa = \frac{PSI}{145.0377}$$

The converted pore pressure data was tabulated and graphed against depth in metres to give a pore pressure against depth for the Carnarvon Basin region.

EFFECTS OF WATER DEPTH

Petroleum wells in the Carnarvon Basin are largely drilled in an oceanic environment (with the exception being the Barrow Island wells. Thus, there is often a large depth of water between the rotary table and the mud line. The water depth has influences the calculation of the vertical stress (Zoback et al. 2003).

1. The water depth is obtained from the individual petroleum wells WCR. The water depth obtained is given in units of metres.
2. To calculate the water depth a constant density is assigned and gravity and depth is used in the following equation.

$$Eq\ 13: Water\ Stress\ (MPa) = ((\frac{waterdepth}{1000}) \times 1.05 \times 9.8)$$

The density of salt water can be assumed to be 1.05 g/cm^3, the water depth is given in metres and the gravity is 9.8 ms^{-2} (Engelder 1993).

NATURAL FRACTURE ANALYSIS

Natural fractures occur in response to the in-situ stress regime, when the rock strength is overcome by the regional stresses. When a rock is under unconfined compression, the rock will deform elastically until failure occurs (Jaeger et al. 1979, Fossen 2010). In a basin environment the fractures focused on are tensile and shear fractures. Shear fractures form 26° to S_{Hmax}, with tensile fractures occurring parallel to the strike of S_{Hmax} (Anderson 1951, Laubach et al. 2004, Laubach et al. 2009). As the Carnarvon Basin has undergone an alternating stress regime for much of its history, fractures can be seen to also associate with palaeo-stress conditions as well as those created by the in-situ stress regime.

Image logs allows for the analysis of the wellbore environment. Natural fractures along with bedding, BOs, DITFs and sedimentary structures can be picked using image logs. Natural fractures, in image logs, appear as sinusoidal, dark or light bands, which crosscut the bedding planes. These differ from DITFs as they are often do not appear vertical or sub-vertical and are not separated by 180° (Brudy et al. 1999b, Zoback et al. 2003). Drilling induced tensile fractures are open at the time of drilling, so they will be in-filled with drilling fluid, so appearing dark or conductive on an image log. Natural

fractures appear in the image log as either electrically conductive or electrically resistive. Drilling induced tensile fractures can be distinguished from natural fractures through their discontinuous structure. Natural fractures appear as continuous sinusoids, while DITFs can be interrupted or separated (Brudy et al. 1999b).

Natural fractures in image logs are identified by continuous or semi-continuous light or dark sinusoids, that cross cut the bedding. Fractures can be interpreted using the sinusoid picking tool provided in JRS Suite.

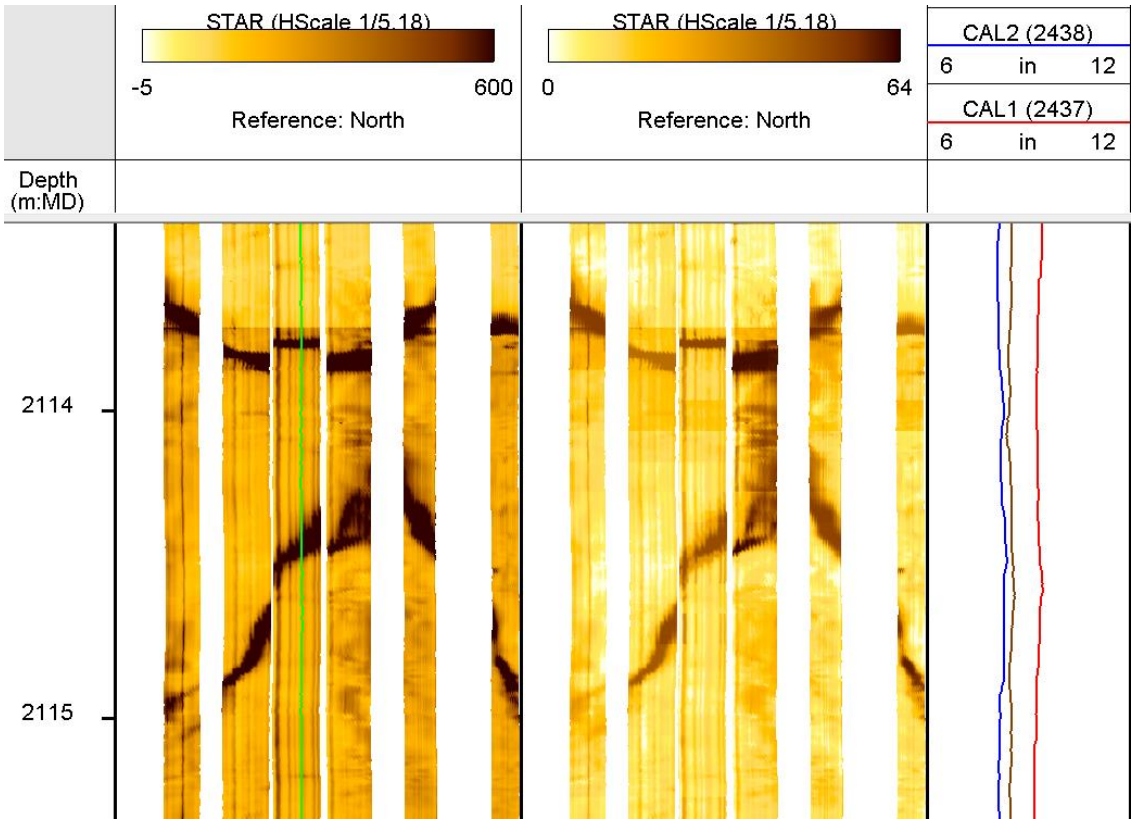

Figure 10: Static and dynamic STAR image logs displaying a conductive fracture in: Skiddaw-2.

Once a natural fracture is identified, it is marked out using the JRS.exe program and labelled as either a conductive fracture or a resistive fracture. This is compiled in the database for further analysis. The fractures are then plotted in Roses JRS Suite© which

plots fractures in bins depending on the density of fractures at a given orientation, along with the dip and dip direction. These fracture roses are displayed in the results section.

APPENDIX 2: WELL INFORMATION CARDS

SHmax Orientation Defined by Bo and DITF

Red SHmax BO: 114.9° Blue SHmax DITF: N/A

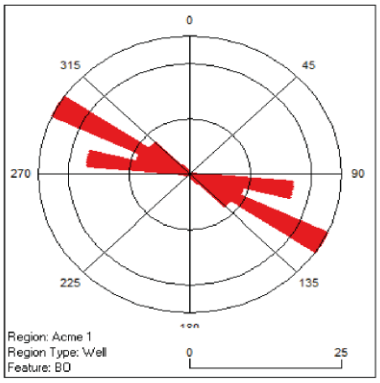

Well Card: Acme-1

	BO	DITF
Number	64	0
Total Length (m)	397.4	0
S.D.	12.2°	0
Quality	A	N/A
SHmax Orientation	114.9°	N/A

BO and DITF Depth vs Azimuth Plot

Red: BO Azimuth

Blue: DITF Azimuth

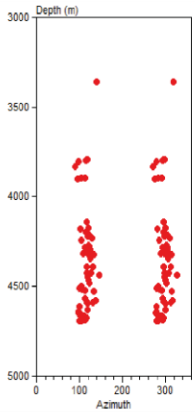

All Fractures

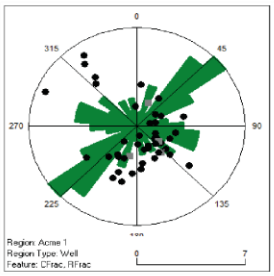

Fracture Dip/DipDirn

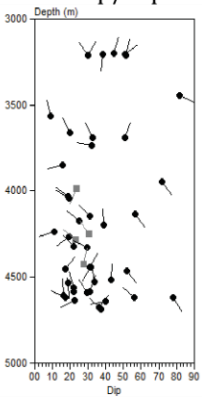

Conductive Fractures

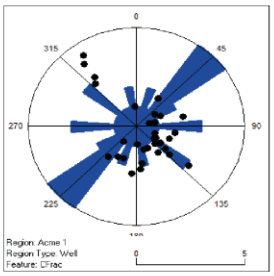

Resistive Fractures

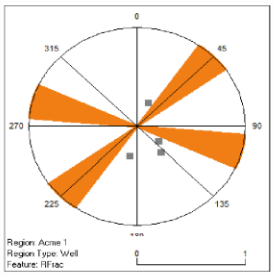

Static and Dynamic Image Log: OBMI

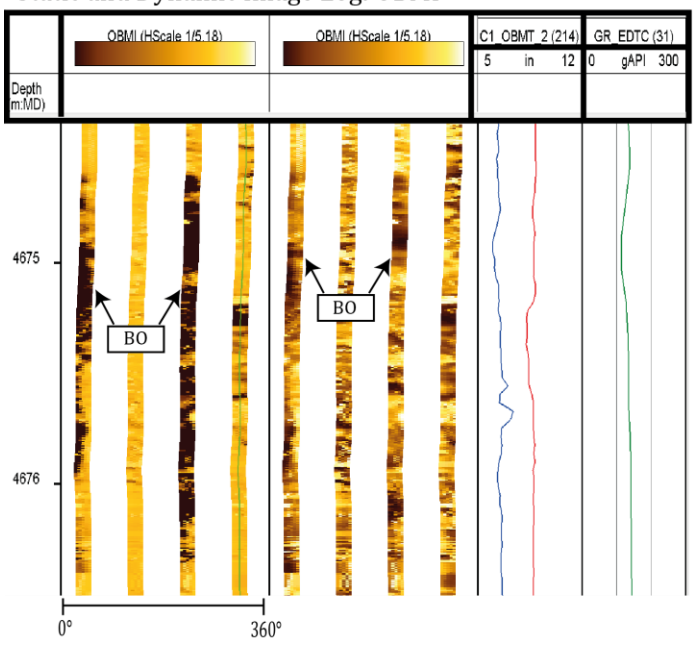

Legend

Latitude:	20°12' 26.9557" S
Longitude	14° 49' 08.7925" E
Image Interval:	3300-4714
RT:	22.3 m
Total Depth:	4715 m
Image Log Type	OBMI
Well Deviation:	<1°
FIT/LOT:	FCP
Density Log:	Yes
Velocity Survey	Yes

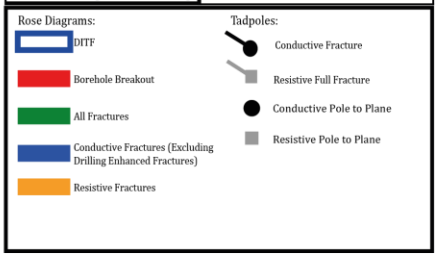

SHmax Orientation Defined by Bo and DITF

Red SHmax BO: 1° Blue SHmax DITF: N/A

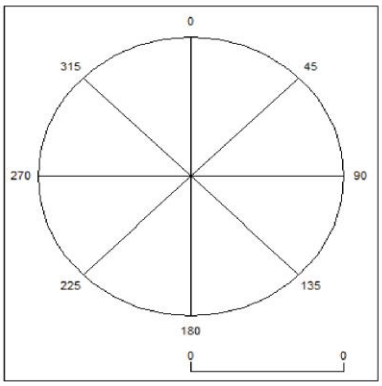

Well Card: Bounty-2

	BO	DITF
Number	0	0
Total Length (m)	0	0
S.D.	0	0
Quality	N/A	N/A
SHmax Orientation	N/A	N/A

BO and DITF Depth vs Azimuth Plot

Red: BO Azimuth

Blue: DITF Azimuth

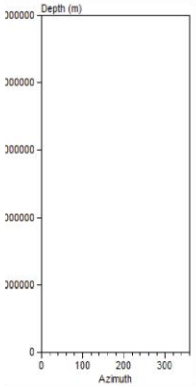

All Fractures

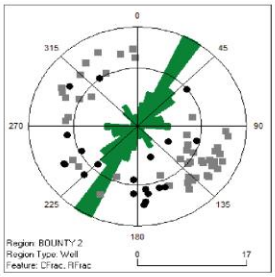

Fracture Dip/DipDirn

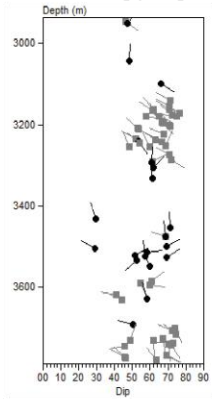

Conductive Fractures

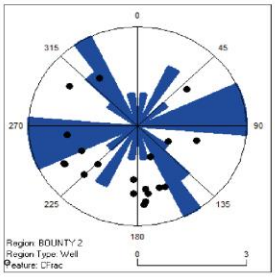

Resistive Fractures

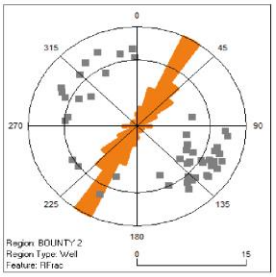

Static and Dynamic Image Log: STAR

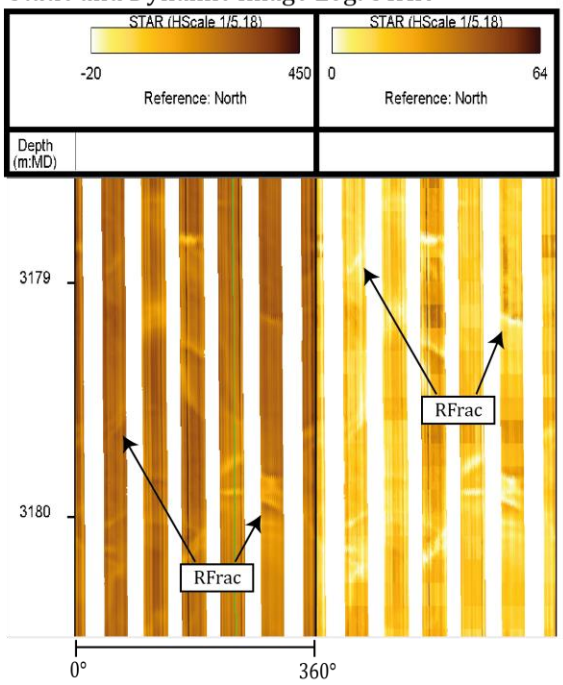

Legend

Latitude:	19° 16' 59.311" S
Longitude	116° 38' 41.148" E
Image Interval:	2852-3795
RT:	22.0 m
Total Depth:	3815.5 m
Image Log Type:	STAR
Well Deviation:	<1°
FIT/LOT:	LOT
Density Log:	Yes
Velocity Survey:	Yes

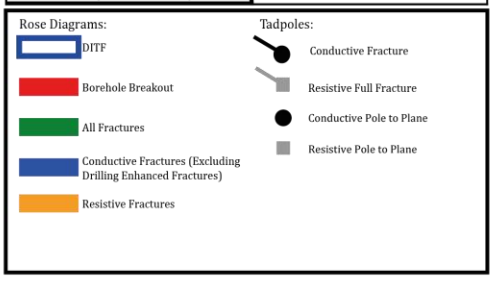

SHmax Orientation Defined by Bo and DITF

Red SHmax BO: 101.8° Blue SHmax DITF: 97.8°

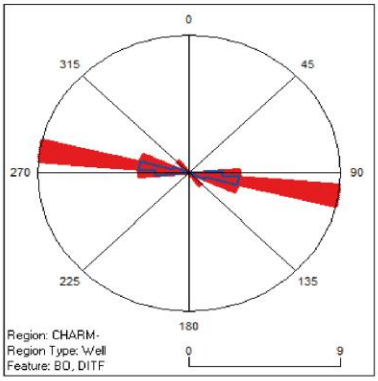

Well Card: Charm-1

	BO	DITF
Number	16	6
Total Length (m)	27.7	21.7
S.D.	10.8°	5.7°
Quality	C	B
SHmax Orientation	101.8°	97.8°

BO and DITF Depth vs Azimuth Plot

Red: BO Azimuth

Blue: DITF Azimuth

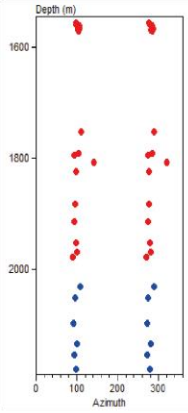

All Fractures

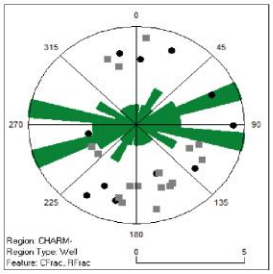

Fracture Dip/DipDirn

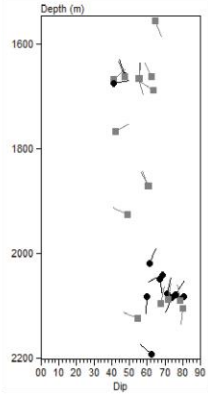

Conductive Fractures

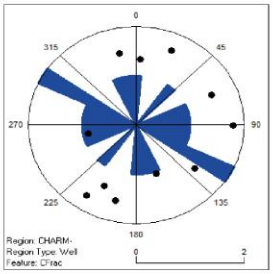

Resistive Fractures

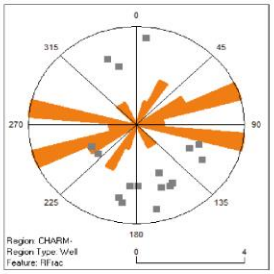

Static Image Log: XRMI

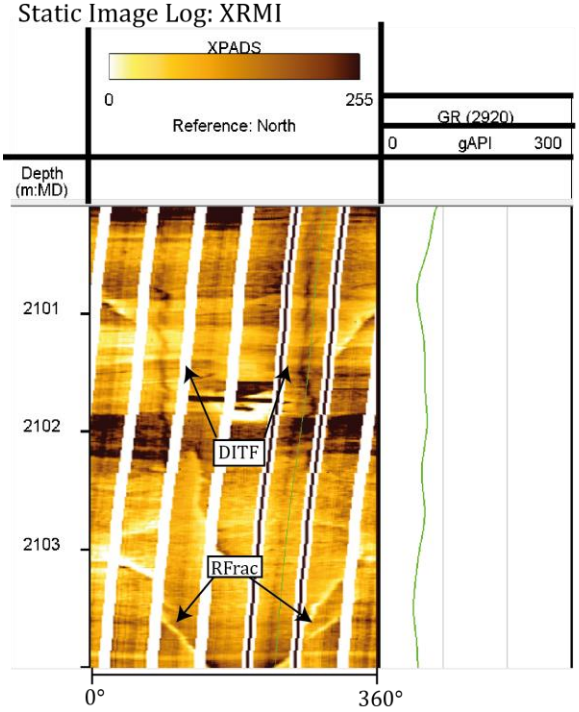

Legend

Latitude:	19° 34' 38.133" S
Longitude	116° 54' 12.987" E
Image Interval:	1540-2232 m
RT:	36.1 m
Total Depth:	2236 m
Image Log Type:	XRMI
Well Deviation:	<5°
FIT/LOT:	LOT
Density Log:	Yes
Velocity Survey:	Yes

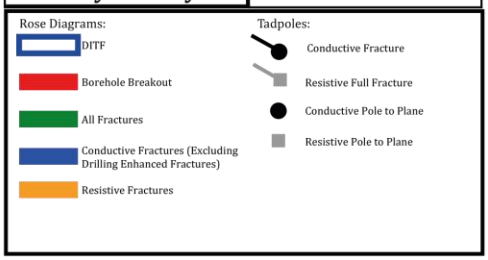

SHmax Orientation Defined by Bo and DITF

Red SHmax BO: N/A Blue SHmax DITF: 119.96°

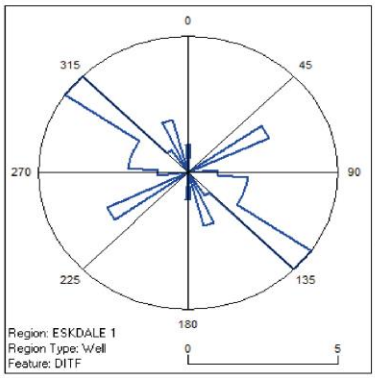

Well Card: Eskdale-1

	BO	DITF
Number	0	25
Total Length (m)	0.0	59.8
S.D.	0	33.8°
Quality	N/A	B
SHmax Orientation	N/A	119.96°

BO and DITF Depth vs Azimuth Plot

Red: BO Azimuth

Blue: DITF Azimuth

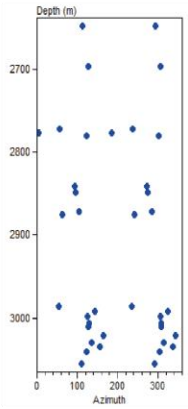

All Fractures

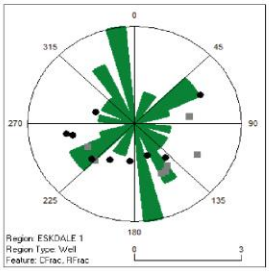

Fracture Dip/DipDirn

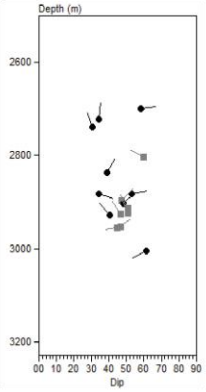

Conductive Fractures

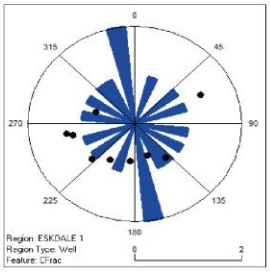

Resistive Fractures

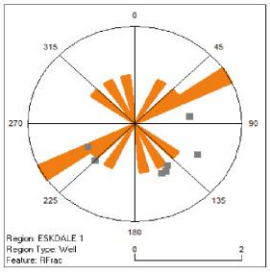

Static and Dynamic Image Log: STAR

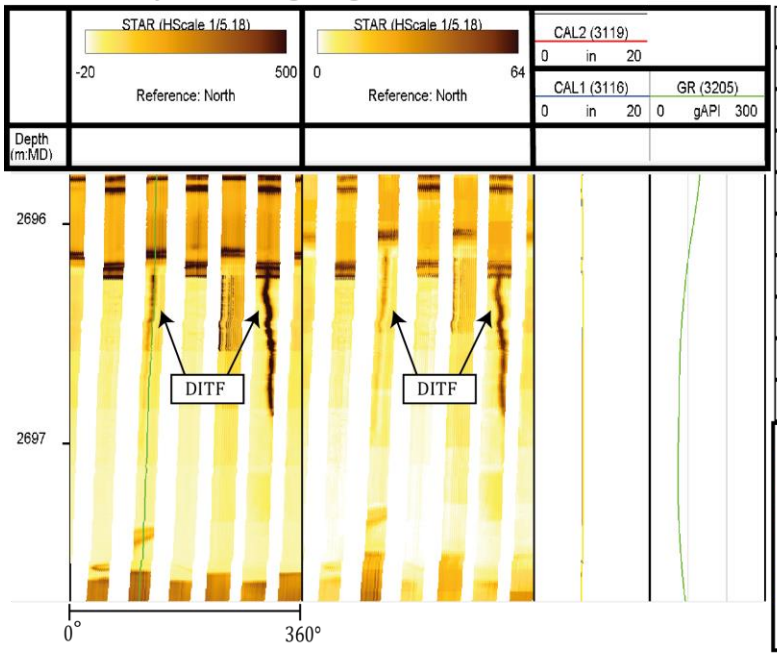

Legend

Latitude:	21° 21' 53.64" S
Longitude	113° 49' 31.74" E
Image Interval:	2640-3065 m
RT:	23.5 m
Total Depth:	3127 m
Image Log Type:	STAR
Well Deviation:	<5°
FIT/LOT:	LOT
Density Log:	Yes
Velocity Survey:	No

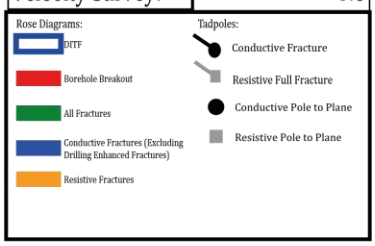

SHmax Orientation Defined by Bo and DITF

Red SHmax BO: 92.5° Blue SHmax DITF: 74.4°

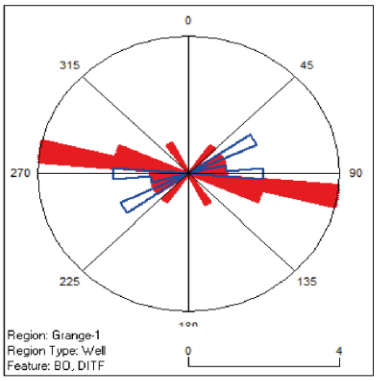

Well Card: Grange-1

	BO	DITF
Number	12	5
Total Length (m)	31.2	7.3
S.D.	27.4°	14.4°
Quality	C	D
SHmax Orientation	92.5°	74.4°

BO and DITF Depth vs Azimuth Plot

Red: BO Azimuth

Blue: DITF Azimuth

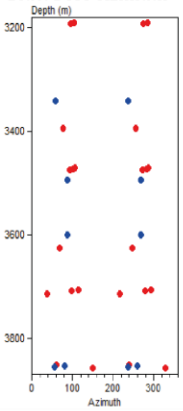

All Fractures

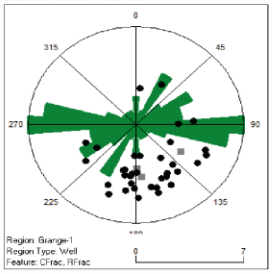

Fracture Dip/DipDirn

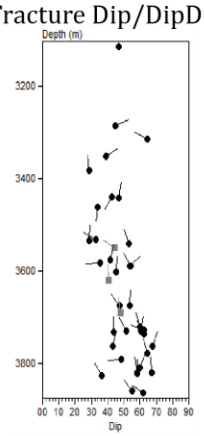

Conductive Fractures

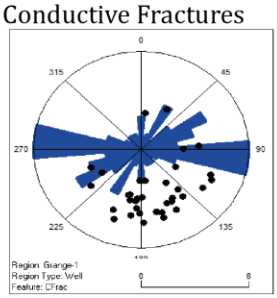

Resistive Fractures

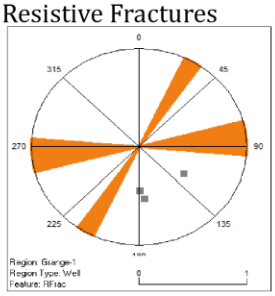

Static and Dynamic Image Log: OBMI

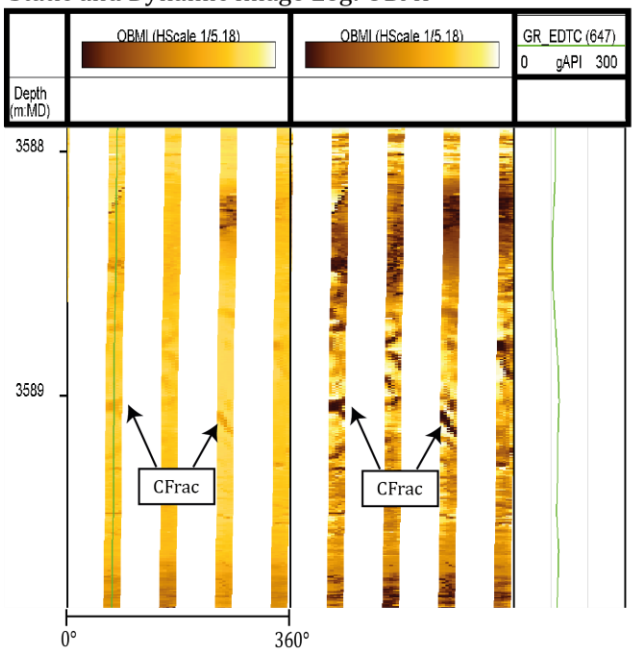

Legend

Latitude:	20° 05' 08.37" S
Longitude	115° 05' 40.74" E
Image Interval:	3088-3858 m
RT:	22.2 m
Total Depth:	3127 m
Image Log Type:	OBMI
Well Deviation:	<1°
FIT/LOT:	LOT
Density Log:	Yes
Velocity Survey:	Yes

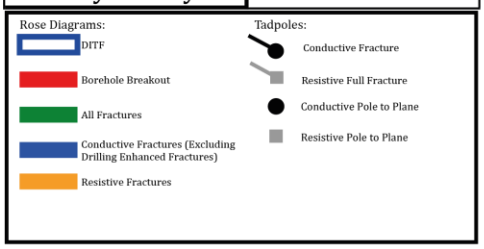

Well Card: Lambert-9

SHmax Orientation Defined by Bo and DITF

Red SHmax BO: 125.1° Blue SHmax DITF: N/A

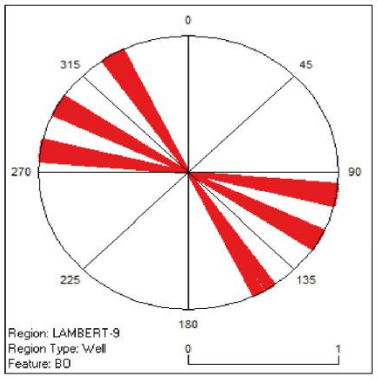

	BO	DITF
Number	3	0
Total Length (m)	1.5	0.0
S.D.	22.6°	0
Quality	E	N/A
SHmax Orientation	125.1°	N/A

BO and DITF Depth vs Azimuth Plot

Red: BO Azimuth

Blue: DITF Azimuth

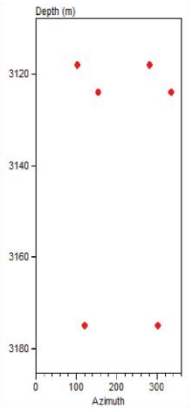

All Fractures

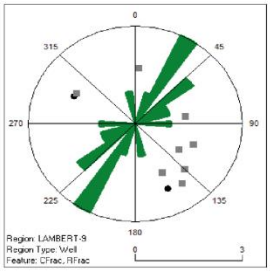

Fracture Dip/DipDirn

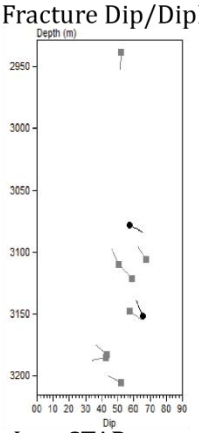

Conductive Fractures

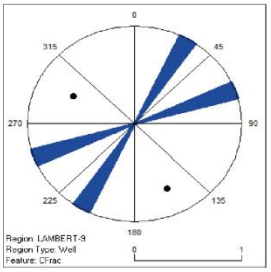

Resistive Fractures

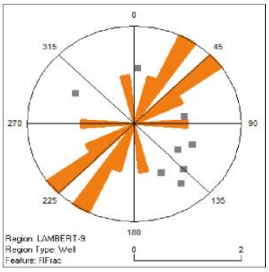

Static and Dynamic Image Log: STAR

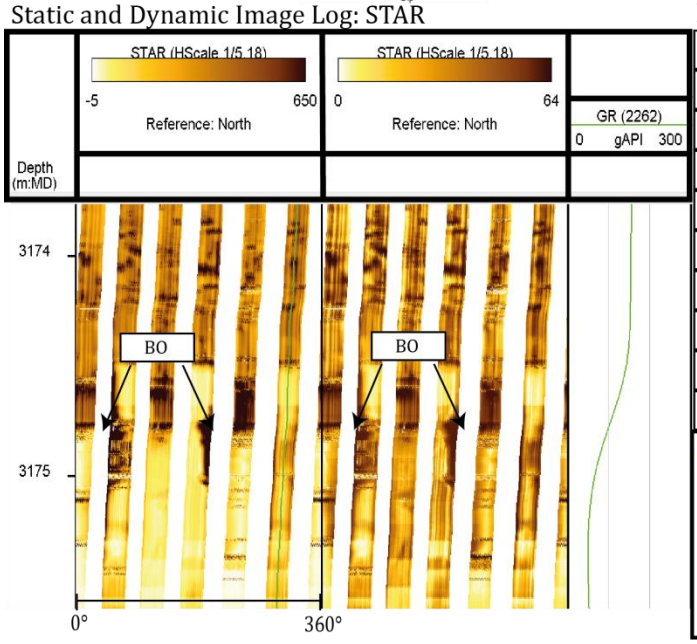

Legend

Latitude:	19° 25' 10.83" S
Longitude	116° 29' 54.38" E
Image Interval:	3209-2916 m
RT:	25 m
Total Depth:	3240 m
Image Log Type:	STAR
Well Deviation:	<5°
FIT/LOT:	LOT
Density Log:	Yes
Velocity Survey:	Yes

Rose Diagrams:
- DITF
- Borehole Breakout
- All Fractures
- Conductive Fractures (Excluding Drilling Enhanced Fractures)
- Resistive Fractures

Tadpoles:
- Conductive Fracture
- Resistive Full Fracture
- Conductive Pole to Plane
- Resistive Pole to Plane

SHmax Orientation Defined by Bo and DITF

Red SHmax BO: 92.5° Blue SHmax DITF: 74.4°

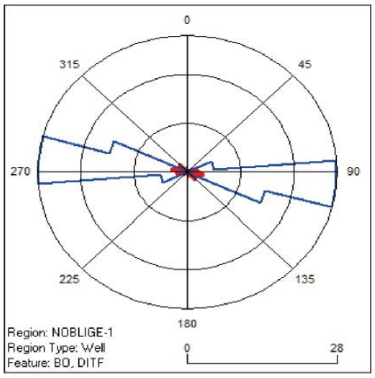

Well Card: Noblige-1

	BO	DITF
Number	14	85
Total Length (m)	12.7	347.9
S.D.	28.5°	11.7°
Quality	D	A
SHmax Orientation	103.6°	96.2°

BO and DITF Depth vs Azimuth Plot

Red: BO Azimuth

Blue: DITF Azimuth

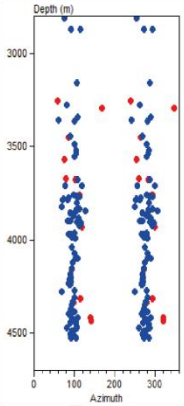

All Fractures

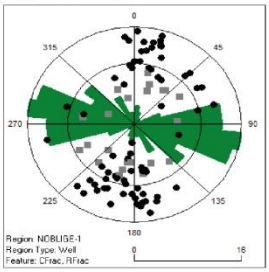

Fracture Dip/DipDirn

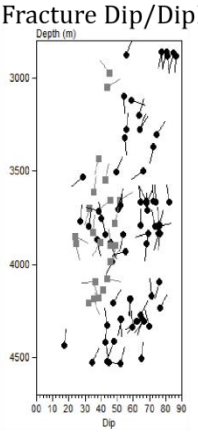

Conductive Fractures

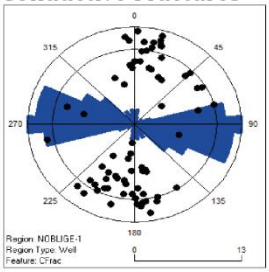

Resistive Fractures

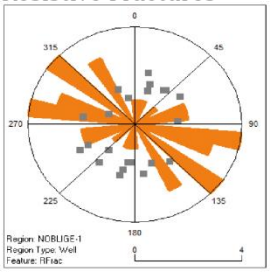

Static and Dynamic Image Log: STAR

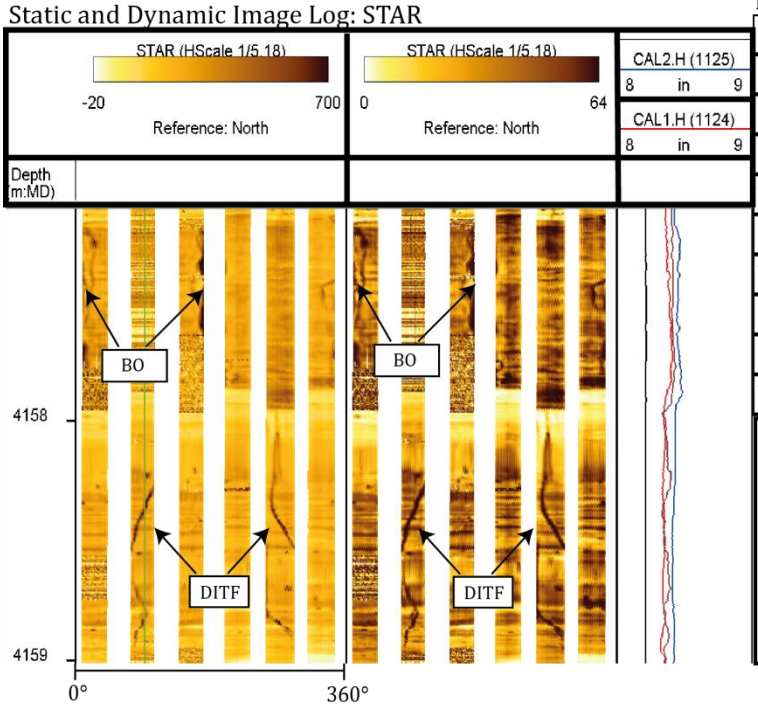

Legend

Latitude:	19° 23' 55.061"S
Longitude	114° 19' 58.698"E
Image Interval:	2700-4571 m
RT:	30.5 m
Total Depth:	4581 m
Image Log Type:	STAR
Well Deviation:	<5°
FIT/LOT:	LOT
Density Log:	Yes
Velocity Survey:	No

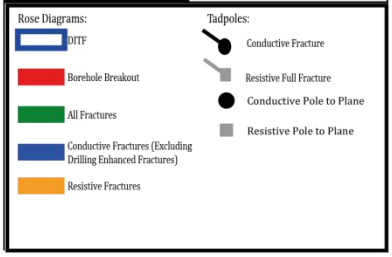

SHmax Orientation Defined by Bo and DITF

Red SHmax BO: 125.6° Blue SHmax DITF: 120.3°

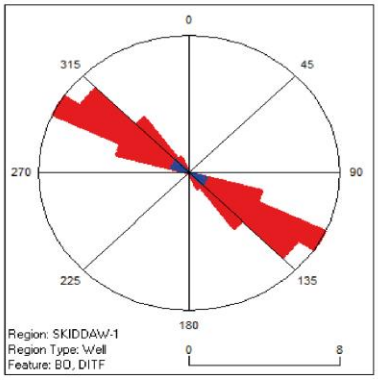

Well Card: Skiddaw-1

	BO	DITF
Number	24	2
Total Length (m)	66.6	3.6
S.D.	10.9°	6.1°
Quality	C	E
SHmax Orientation	125.6°	120.3°

BO and DITF Depth vs Azimuth Plot

Red: BO Azimuth

Blue: DITF Azimuth

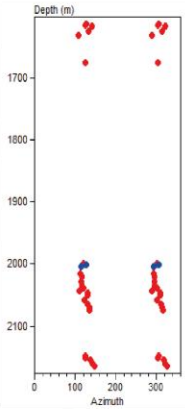

All Fractures

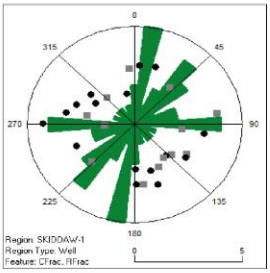

Fracture Dip/DipDirn

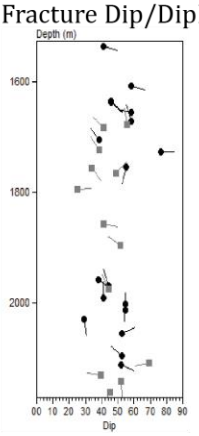

Conductive Fractures

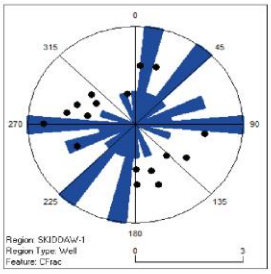

Resistive Fractures

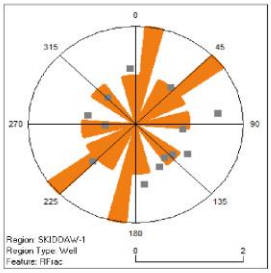

Static and Dynamic Image Log: STAR

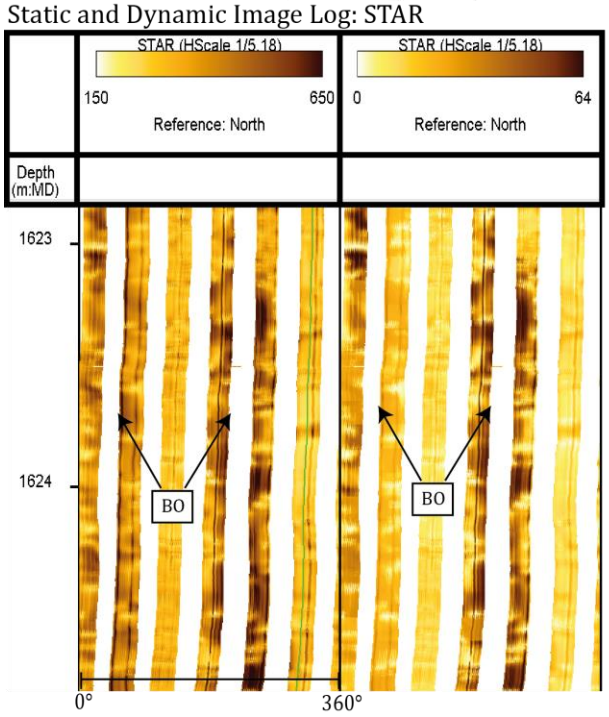

Legend

Latitude:	-21.48045
Longitude	113.871903°
Image Interval:	1504-2180 m
RT:	N/A
Total Depth:	N/A
Image Log Type:	STAR
Well Deviation:	<5°
FIT/LOT:	N/A
Density Log:	Yes
Velocity Survey:	Yes

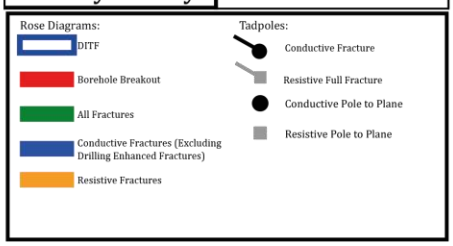

SHmax Orientation Defined by Bo and DITF

Red SHmax BO: 126.8° Blue SHmax DITF: 127.6°

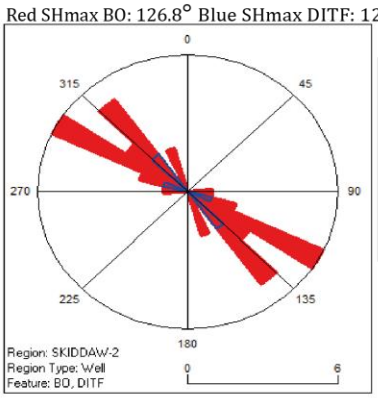

Well Card: Skiddaw-2

	BO	DITF
Number	20	3
Total Length (m)	28.9	10.5
S.D.	17.4°	13.7°
Quality	C	D
SHmax Orientation	126.8°	127.6°

BO and DITF Depth vs Azimuth Plot

Red: BO Azimuth
Blue: DITF Azimuth

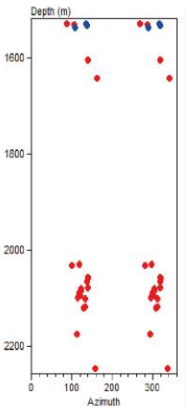

All Fractures

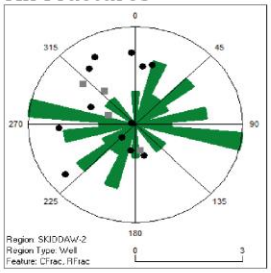

Fracture Dip/DipDirn

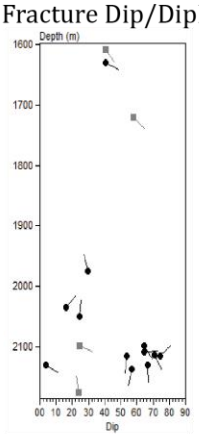

Conductive Fractures

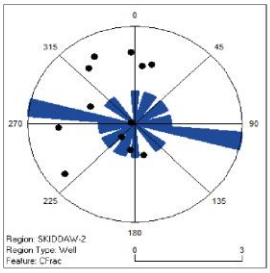

Resistive Fractures

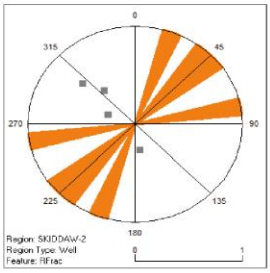

Static and Dynamic Image Log: STAR

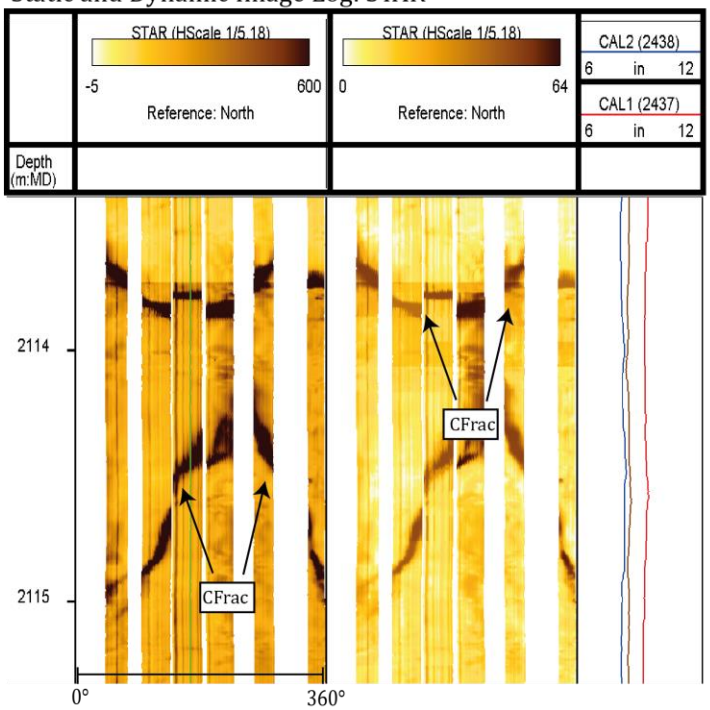

Legend

Latitude:	-21.48045°
Longitude	113.871903°
Image Interval:	1509-2249 m
RT:	N/A
Total Depth:	N/A
Image Log Type:	STAR
Well Deviation:	<5°
FIT/LOT:	N/A
Density Log:	Yes
Velocity Survey:	No

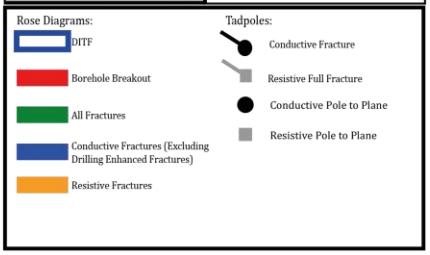

SHmax Orientation Defined by Bo and DITF

Red SHmax BO: 135.2° Blue SHmax DITF: N/A

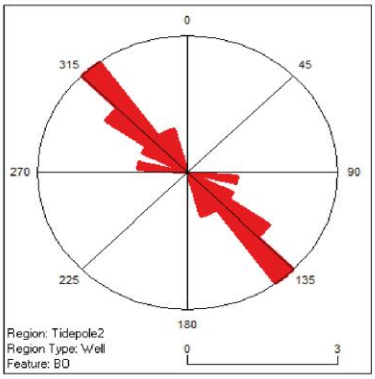

Well Card: Tidepole-2

	BO	DITF
Number	9	0
Total Length (m)	20.0	0.0
S.D.	16.8°	0°
Quality	D	N/A
SHmax Orientation	135.2°	0°

BO and DITF Depth vs Azimuth Plot

Red: BO Azimuth

Blue: DITF Azimuth

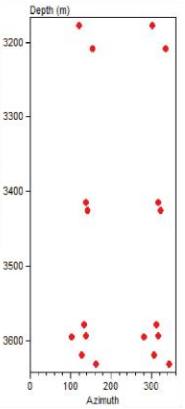

All Fractures

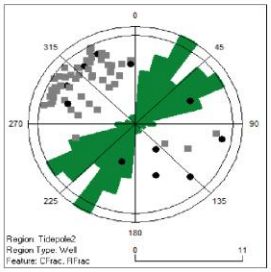

Fracture Dip/DipDirn

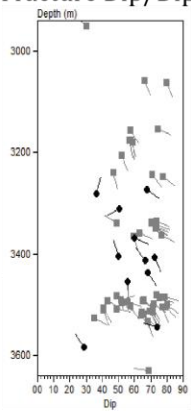

Conductive Fractures

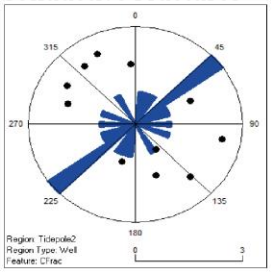

Resistive Fractures

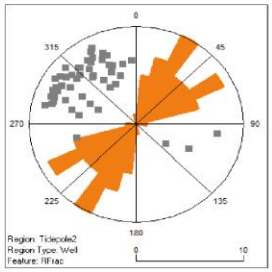

Static and Dynamic Image Log: STAR

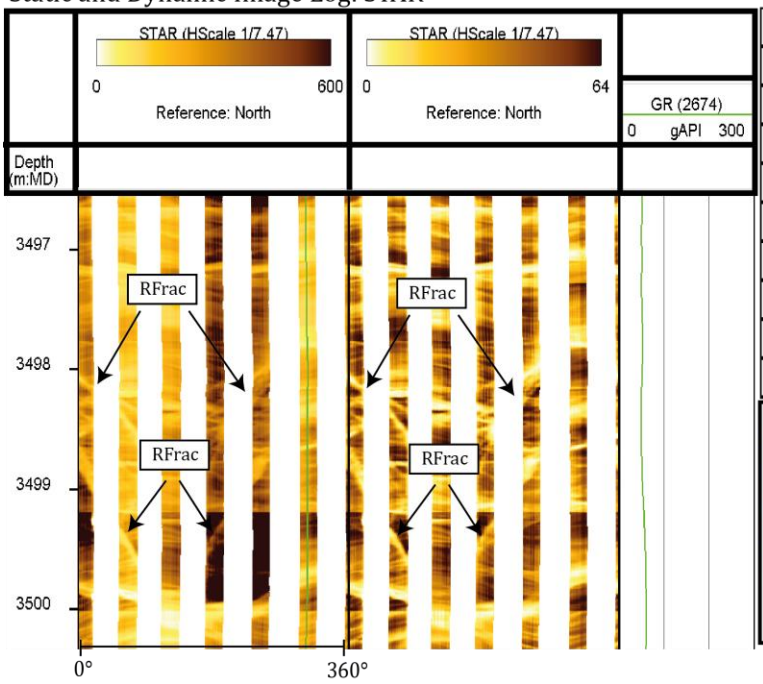

Legend

Latitude:	19° 45' 25.80"S
Longitude	115° 53' 19.11"E
Image Interval:	2880-3660 m
RT:	25 m
Total Depth:	3718 m
Image Log Type:	STAR
Well Deviation:	<10°
FIT/LOT:	FIT
Density Log:	Yes
Velocity Survey:	No

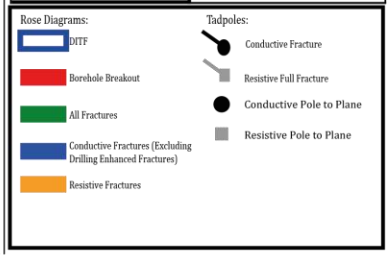

SHmax Orientation Defined by Bo and DITF

Red SHmax BO: N/A Blue SHmax DITF: N/A

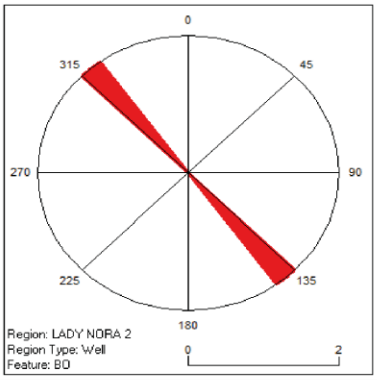

Well Card: Lady Nora-2

	BO	DITF
Number	2	0
Total Length (m)	1.7	0.0
S.D.	0.25°	0
Quality	E	N/A
SHmax Orientation	142.5°	N/A

BO and DITF Depth vs Azimuth Plot

Red: BO Azimuth

Blue: DITF Azimuth

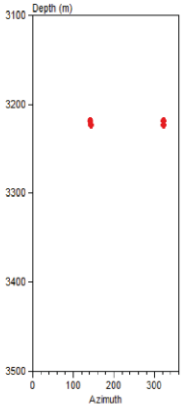

All Fractures

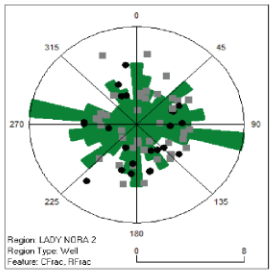

Fracture Dip/DipDirn

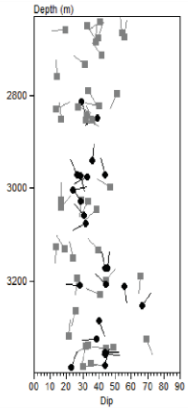

Conductive Fractures

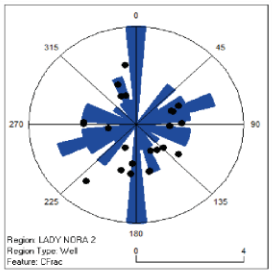

Resistive Fractures

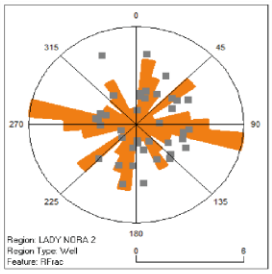

No Image Log Available

Legend

Latitude:	19° 49' 59.82" S
Longitude	115° 37' 14.44" E
Image Interval:	2660-3419 m
RT:	25 m
Total Depth:	3425 m
Image Log Type:	STAR
Well Deviation:	<5°
FIT/LOT:	LOT
Density Log:	Yes
Velocity Survey:	No

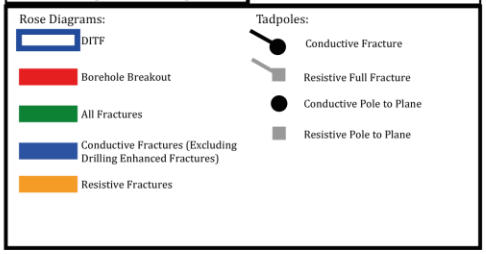

APPENDIX 3: DENSITY LOG

Well	DENSITY LOGS				VSP Present
	Log Present	Top	Bottom	Interval	
Bleaberry West-1	Yes	1240	1592	352	Yes
Lambert-8	No			0	Yes
Amulet-1	Yes	1090.9	1882.95	792.05	No
Charm-1	Yes	1170	2220.4	1050.4	Yes
Chandon-2	Yes	1168.603	2597.963	1429.36	Yes
Balnaves Deep-1	No			0	Yes
Beg-1	No				Yes
Blackdragon-1	Yes	2397.252	2536.008	138.756	Yes
Bounty-2	Yes	2150.97	3791.712	1640.742	Yes
Crosby-1	No			0	No
Eskdale-1	No			0	No
Glenloth-1	Yes	4876.343	4959.401	83.0581	Yes
Grange-1	Yes	1983.028	3847.642	1864.614	Yes
Iago-5	Yes	1491.386	3638.398	2147.012	Balnaves Deep
Kentish Knock-1	No			0	Yes
Lady Nora - 2	Yes	2013.204	3397.91	1384.706	Balnaves Deep
Lambert-8	No			0	Yes
Lambert-9	Yes	2024.786	3214.421	1189.634	Yes
Libris-1	Yes	3222.346	3393.338	170.9924	Yes
Maitland-1	Yes	975.0552	1314.907	339.852	Yes
Marley-1	Yes	2394.052	3061.259	667.2072	No
Noblige-1	Yes	2415.692	4559.198	2143.506	Yes
Okapi-1	Yes	900.0744	1379.22	479.1456	Yes
Salsa-1	Yes	2907.5	3128.6	221.1	Yes
Sappho-1	No			0	Yes
Scalybutt-1	Yes	2057.857	2868.016	810.1584	Yes
Skiddaw-1	Yes	1477.06	2152.04	674.9804	Yes
Skiddaw-2	Yes	1472.794	2227.326	754.532	No
Stybarrow-1	No			0	No
Stybarrow-2	Yes	2032.406	2147.468	115.062	Yes
Supel-1	No			0	Yes
Taunton-4	Yes (SBD2)	651.1	1401.1	750	No
Thomas Bright-1	No	0			Yes
Tidepole-2	Yes	1964.741	3672.383	1707.642	Lambert-8
Wheatstone-4	Yes	1153.82	3553.054	2399.233	Balnaves Deep